Author Manuscript

Author Manuscript

Author Manuscript

Author Manuscript

HHS Public Access

Author manuscript

Cell Rep. Author manuscript; available in PMC 2019 June 09.

Published in final edited form as:

Cell Rep. 2019 April 16; 27(3): 860–871.e8. doi:10.1016/j.celrep.2019.03.072.

Overlapping Activities of Two Neuronal Splicing Factors Switch the GABA Effect from Excitatory to Inhibitory by Regulating REST

Yoko Nakano[1,2], **Susan Wiechert**[1,2], and **Botond Bánfi**[1,2,3,4,5,*]

[1]Department of Anatomy and Cell Biology, Carver College of Medicine, University of Iowa, Iowa City, IA 52242, USA

[2]Inflammation Program, Carver College of Medicine, University of Iowa, Iowa City, IA 52242, USA

[3]Department of Otolaryngology—Head and Neck Surgery, Carver College of Medicine, University of Iowa, Iowa City, IA 52242, USA

[4]Department of Internal Medicine, Carver College of Medicine, University of Iowa, Iowa City, IA 52242, USA

[5]Lead Contact

SUMMARY

A truncating mutation in the mouse *Srrm4* gene, which encodes a neuronal splicing factor, causes alternative splicing defects selectively in the ear. The mechanism by which splicing is preserved in the brain of these mice is not known. Here, we show that SRRM3 limits the *Srrm4* mutation-associated defects to the ear and that, in cortical neurons, overlapping SRRM3-SRRM4 activity regulates the development of interneuronal inhibition. *In vitro*, SRRM3 and SRRM4 regulate the same splicing events, but a mutation in mouse *Srrm3* causes tremors and mild defects in neuronal alternative splicing, demonstrating unique SRRM3 roles *in vivo*. Mice harboring mutations in both *Srrm3* and *Srrm4* die neonatally and exhibit severe splicing defects. In these mice, splicing alterations prevent inactivation of the gene repressor REST, which maintains immature excitatory GABAergic neurotransmission by repressing *K-Cl cotransporter* 2. Thus, our data reveal that SRRM3 and SRRM4 act redundantly to regulate GABAergic neurotransmission by inactivating REST.

Graphical Abstract

*Correspondence: botond-banfi@uiowa.edu.

AUTHOR CONTRIBUTIONS

Y.N., B.B., and S.W. performed the experiments. Y.N. and B.B. designed the experiments, analyzed the data, and wrote the manuscript.

SUPPLEMENTAL INFORMATION

Supplemental Information can be found online at https://doi.org/10.1016/j.celrep.2019.03.072.

DECLARATION OF INTERESTS

The authors declare no competing interests.

Author Manuscript Author Manuscript Author Manuscript Author Manuscript

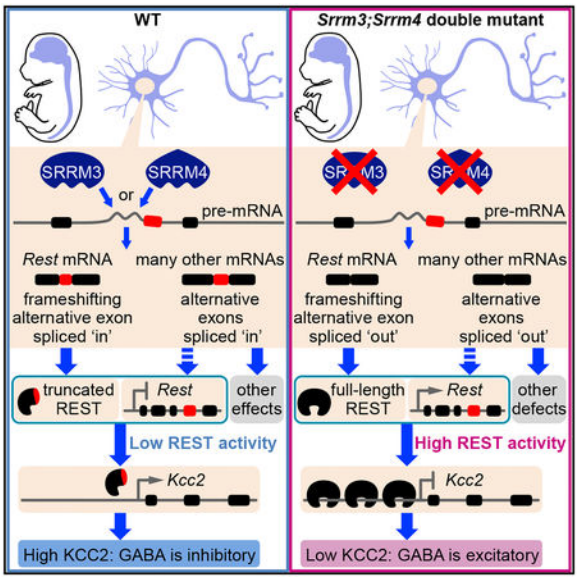

In Brief

Nakano et al. report that the paralogous proteins SRRM3 and SRRM4 regulate the alternative splicing of overlapping groups of exons in the CNS and that the SRRM3-SRRM4-regulated splicing alterations change GABAergic neurotransmission from excitatory to inhibitory during development by inactivating the gene repressor REST and derepressing its target gene *Kcc2*.

INTRODUCTION

The *K-Cl cotransporter 2* gene (*Kcc2*) encodes a Cl^-exporter that is critical for inhibitory GABAergic neurotransmission (Ben-Ari et al., 2007). In immature neurons, *Kcc2* expression is low, and the cytosolic concentration of $Cl^-$is high. In these cells, gamma-aminobutyric acid (GABA) acts as an excitatory neuro-transmitter because Cl^- is driven out of the cell through the ligand-gated Cl^-channel GABA type A receptor ($GABA_AR$) by its high cytosolic concentration (Rivera et al., 1999). During neuronal development, upregulation of *Kcc2* leads to a reduction in the concentration of intracellular Cl^-. This change in Cl^-concentration switches the effect of GABA from excitatory to inhibitory because it reverses the direction of the GABA-induced Cl^- flux (Rivera et al., 1999). The KCC2-dependent switch in GABAergic neurotransmission is physiologically important because abnormally low KCC2 activity is associated with excitatory GABA effects and early-onset epilepsy in both humans and mice (Moore et al., 2017).

Kcc2 and hundreds of other neuronal genes are repressed in non-neuronal cells by the RE1-silencing transcription factor REST (Karadsheh and Delpire, 2001; Bruce et al., 2004). In differentiating neurons, REST activity is reduced, and the target genes of REST are upregulated. The upregulation of *Kcc2* and many other REST target genes can be prevented in primary cultures of differentiating neurons by overexpressing REST from a plasmid. In these REST-transfected cells, abnormally low *Kcc2* expression maintains the immature, excitatory effect of GABA (Yeo et al., 2009). Thus, endogenous and neuron-specific

Author Manuscript Author Manuscript Author Manuscript Author Manuscript

regulators of REST may indirectly affect the development of inhibitory GABAergic neurotransmission.

Transcriptional repression is the main mechanism whereby REST is downregulated in differentiating neurons (Ballas et al., 2005); however, REST is also inactivated through the alternative splicing of a frameshift-causing exon (i.e., exon 4) into its mRNA. This splicing event truncates REST upstream of a repressor domain and three zinc-finger domains that are critical for its gene silencing function. The splicing of exon 4 into *Rest* is selective to a few cell types, including neurons, mechanosensory hair cells of the ear, and some cancer cells (Palm et al., 1999; Nakano et al., 2012). Exon 4 splicing into *Rest* requires the Ser-Arg-rich splicing factor SRRM4 in hair cells and some neuroblastoma cancer cells and neuroendocrine tumors (Raj et al., 2011; Nakano et al., 2012; Li et al., 2017). In hair cells, the SRRM4-truncating mutation of Bronx waltzer ($Srrm4^{bv/bv}$) mice prevents incorporation of exon 4 into *Rest* and causes further splicing defects in 50 other transcripts. Although *Srrm4* is also expressed in neurons, splicing alterations were not detected in the brain of $Srrm4^{bv/bv}$ mice on postnatal day 15 (P15) (Nakano et al., 2012). Consistent with these transcriptome data, the $Srrm4^{bv/bv}$ mouse is characterized by normal brain histology and perinatal degeneration of most hair cells. The mechanism whereby the alternative splicing of *Rest* and other pre-mRNA targets of SRRM4 are maintained in the brain of $Srrm4^{bv/bv}$ mice is not known. In fact, the necessity of SRRM4 for the alternative splicing of *Rest* in neurons is unclear.

To identify the regulators of alternative splicing of *Rest* in neurons, we examined the mechanism by which incorporation of exon 4 into *Rest* is maintained in the brain of $Srrm4^{bv/bv}$ mice. We reanalyzed previous microarray data from $Srrm4^{bv/bv}$ mice (Nakano et al., 2012) and found that the $Srrm4^{bv/bv}$ genotype is associated with reduced expression of the *Srrm4* paralog *Srrm3* in the inner ear but not the brain. Based on this observation, we tested the functions of SRRM3 in wild-type (WT) and $Srrm4^{bv/bv}$ mice. In WT mice, SRRM3 was required for motor coordination, whereas in $Srrm4^{bv/bv}$ mice, SRRM3 was necessary for the survival of newborns. In cortical neurons, SRRM3 and SRRM4 acted redundantly to regulate many alternative splicing events, including splicing of exon 4 into *Rest*. Moreover, the SRRM3-SRRM4-regulated inactivation of REST was necessary for the KCC2-dependent switch in GABAergic neurotransmission. Thus, our data reveal that SRRM3-SRRM4 activity downregulates REST to switch GABAergic neuro-transmission from excitatory to inhibitory.

RESULTS

SRRM3 Exhibits SRRM4-like Activity in Transfected Cells

We reported previously that SRRM4-like activity is present in the brain of $Srrm4^{bv/bv}$ mice on P15 (Nakano et al., 2012). To determine whether the SRRM4-like activity was also present at earlier times during brain development, we selected exon 4 of *Rest* and four other alternative exons that are regulated by SRRM4 in the inner ear and used RT-PCR to analyze their splicing in the neocortex of WT and $Srrm4^{bv/bv}$ mice on embryonic day 14 (E14), E16.5, P0, and P16 (Figures 1A and S1A). RNA isolated from the inner ear of WT and $Srrm4^{bv/bv}$ mice on E16.5 served as reference samples for the evaluation of SRRM4 activity.

Author Manuscript Author Manuscript Author Manuscript Author Manuscript

This analysis revealed that all five exons were spliced into the mRNA at abnormally low rates in the inner ear of *Srrm4*$^{bv/bv}$ mice, whereas in the neocortex, the splicing of only three of these five exons was abnormal (Figures 1A and S1A). Moreover, the splicing defects of those three exons were mild and temporary; no splicing alterations were detected on P16 (Figure 1B). Thus, the SRRM4-like activity observed in *Srrm4*$^{bv/bv}$ mice increases during cortical development.

To identify the source of the SRRM4-like activity, we searched for *Srrm4* paralogs present in the neocortex but absent from the inner ear of *Srrm4*$^{bv/bv}$ mice. Blast searches with SRRM4 showed that it is similar to the ubiquitously expressed splicing factors SRRM1 and SRRM2 as well as to SRRM3 (Figure 1C), whose tissue distribution has not been examined. Reanalysis of previously published microarray datasets (Nakano et al., 2012) suggested that the expression of *Srrm3* was reduced in the inner ear but not the brain of *Srrm4*$^{bv/bv}$ mice. qRT-PCR analysis of the inner ear and brain of WT and *Srrm4*$^{bv/bv}$ mice on E16.5 confirmed the microarray data (Figure S1B). Further RT-PCR tests revealed that *Srrm3* was expressed selectively in neural tissues and neuronal cell lines (Figures 1D and S1C). In addition, duplex *in situ* hybridization of brain sections with probes complementary to *Srrm3* and the neuronal mRNA *Rbfox3* demonstrated that *Srrm3* expression was specific to neurons (Figures 1E and S1D). qRT-PCR analysis of the neocortex of WT mice at multiple developmental stages revealed that the cortical expression of *Srrm3* increased from E14 to P16, whereas that of *Srrm4* somewhat decreased (Figure 1F). Thus, lessening the splicing defects in the neocortex of *Srrm4*$^{bv/bv}$ mice coincides with developmental upregulation of *Srrm3*.

The SRRM3 protein contains predicted nuclear localization signals, Ser-Arg-rich segments, and two regions of particularly high similarity with SRRM4 (Figure S1E). To test for similarities in the molecular functions of SRRM3 and SRRM4, we cotransfected HEK293 cells with an expression vector encoding SRRM3, SRRM4, a distantly related splicing factor (i.e., SRSF1), or no insert (vector control) plus one of three minigene constructs (splicing reporters). In each minigene, constitutive exons flanked an ~800-bp genomic region that contains an SRRM4-regulated exon and its neighboring intronic sequences (Figure 1G). RT-PCR analysis revealed that both SRRM3 and SRRM4 enhanced the incorporation of minigene-encoded alternative exons into the mRNAs, whereas heterologous SRSF1 had no effect (Figure 1G). The slightly higher activity of SRRM4 versus SRRM3 correlated with the difference in expression of the two proteins (Figure S1F). Moreover, RT-PCR analysis of a set of mutated minigene-encoded mRNAs revealed that the same intronic UGC motifs were necessary for SRRM3-dependent splicing (Figure S1G) as those that recruit SRRM4 to the pre-mRNA (Nakano et al., 2012; Raj et al., 2014). Together, these results demonstrate that SRRM3 is a neuronal splicing regulator that has SRRM4-like activity in transfected cells.

SRRM3 Regulates Neuronal Alternative Splicing of Several Transcripts

To evaluate the function of SRRM3, we used *Srrm3* gene-trapped (*Srrm3*$^{gt/gt}$) mice. The gene trap is located in the third intron of *Srrm3*, and it encodes a β-galactosidase reporter (Figure 2A). RT-PCR testing of five brain regions of WT and *Srrm3*$^{gt/gt}$ mice demonstrated

Author Manuscript Author Manuscript Author Manuscript Author Manuscript

that the gene trap prevented expression of *Srrm3* (Figures 2A and S2A). *Srrm3*$^{+/gt}$ mice exhibited no apparent neurological defects, whereas *Srrm3*$^{gt/gt}$ mice were characterized by decreased body size (Figure 2A), reduced lifespan, impaired motor coordination, ataxia, and tremors (Figures S2B–S2E; Video S1). Thus, the loss of *Srrm3* expression disrupts growth, movement, and survival in mice.

We took advantage of the β-galactosidase reporter to evaluate the promoter activity of *Srrm3* in the *Srrm3*$^{+/gt}$ mouse brain. β-Galactosidase activity was detected throughout the brain, with the highest intensities in the neocortex, collicular midbrain tectum, and cerebellum (Figures S2F and S2G). Given the critical role of the cerebellum in motor coordination, we analyzed cerebellum histology in *Srrm3*$^{gt/gt}$ mice. Although the overall structure of the cerebellum was unaltered on P16, the external germinal layer, which forms from granule cell precursors during development, persisted longer than normal (Figure S2H–S2K). Furthermore, most Purkinje cells degenerated in *Srrm3*$^{gt/gt}$ mice between P40 and P90 (Figures S2L–S2O). Histological analysis of the brain cortex did not reveal neurodegeneration (Figure S2P). These data demonstrate that SRRM3 is critical for Purkinje cell survival.

We used mouse exon junction arrays (MJAYs) for transcriptome-wide analysis of alternative splicing in the cerebellum of WT and *Srrm3*$^{gt/gt}$ mice on P16. This analysis revealed 177 potential splicing defects in *Srrm3*$^{gt/gt}$ mice (Figure 2B; Table S1). Of these, 57 defects were tested using RT-PCR, and 88% of these were validated (Figures 2C, S3A, and S3G; Table S1). The majority of splicing defects reduced the ratio of alternative exon-containing to alternative exon-omitting isoforms, suggesting that certain exons were skipped at an abnormally high rate during pre-mRNA splicing in *Srrm3*$^{gt/gt}$ mice. Most of the SRRM3-regulated exons were short, flanked by highly conserved intronic sequences, and incorporated into the mRNA only in neural tissues of WT mice (Figures 2B, S3B, and S3C). RT-PCR analysis of the splicing of five SRRM3 target exons in the neocortex of WT and *Srrm3*$^{gt/gt}$ mice demonstrated that SRRM3 also regulated alternative splicing in the neocortex (Figure S3D). Thus, SRRM3 regulates the splicing of a set of alternative exons in the brain.

Comparing the splicing defects in the inner ear of *Srrm4*$^{bv/bv}$ mice and the cerebellum of *Srrm3*$^{gt/gt}$ mice revealed that in the cerebellum, SRRM3 was required for the splicing of 31% of exons that are SRRM4-regulated in the inner ear (Table S1). Most of these common exon targets of SRRM3 and SRRM4 were encoded by genes whose transcripts were more strongly detected in the Purkinje cell layer than in other cerebellar layers in previous high-throughput *in situ* hybridization assays (Lein et al., 2007; Figure S3E). Therefore, we also compared the cerebellar expression patterns of *Srrm3* and *Srrm4* in WT mice using *in situ* hybridizations. These assays revealed a strong *Srrm3* signal in all three cerebellar layers, whereas the *Srrm4* signal was weak in Purkinje cells and strong in cells of the granular and molecular layers (Figures 2D and S3F). RT-PCR analysis of laser capture microdissected Purkinje and granular layers from WT and *Srrm3*$^{gt/gt}$ mice demonstrated that the *Srrm3*$^{gt/gt}$ genotype was associated with more severe splicing defects in the Purkinje layer than in the granular layer (Figure S3G). Furthermore, RT-PCR analysis of the Purkinje layer of *Srrm3*$^{gt/gt}$ mice identified mild splicing defects for additional SRRM4-regulated exons that

Author Manuscript Author Manuscript Author Manuscript Author Manuscript

were not differentially spliced in the granular layer of WT versus *Srrm3*$^{gt/gt}$ mice (Figure 2E). These data suggest that SRRM4 limits the severity of splicing defects in *Srrm3*$^{gt/gt}$ mice.

SRRM3 and SRRM4 Activities Overlap *In Vivo*

To evaluate the extent to which SRRM4 limits the molecular and phenotypic alterations in *Srrm3*$^{gt/gt}$ mice, we intercrossed the *Srrm3*$^{+/gt}$ and *Srrm4*$^{bv/bv}$ mouse lines and generated double mutant (dMut; i.e., *Srrm3*$^{gt/gt}$;*Srrm4*$^{bv/bv}$) mice. The dMut mice were born from *Srrm3*$^{+/gt}$;*Srrm4*$^{bv/bv}$ breeding pairs at the expected Mendelian ratio (Figure S4A), were normal in size (Figure 2F), and had a beating heart at birth. However, none of the newborn dMut mice started to breathe (Figure S4A). H&E staining of lung sections confirmed that, in dMut mice, but not in their control littermates, the alveoli were never expanded with air (Figure 2F). Thus, the dMut phenotype is much more severe than the individual phenotypes of *Srrm3*$^{gt/gt}$ and *Srrm4*$^{bv/bv}$ mice.

Nissl staining did not reveal anatomical defects in the brain of dMut mice on E19 (Figure S4B). Based on its volume and developmental stage on E19, we selected the neocortex for MJAY-based comparison of alternative splicing in WT and dMut mice. More than 370 potential splicing differences were identified (Figure 2G; Table S2). Of these, 106 defects were tested using RT-PCR, and 89% of the 106 were validated (Figures 2H, S4C, and S4D). The majority of SRRM3-SRRM4-regulated exons were spliced into mRNA only in neural tissues of WT mice (Figure 2G) and were flanked by highly conserved intronic sequences (Figure S4E), and 58% were microexons (i.e., 3–30 nt long) (Figure S4F).

Comparison of the splicing defects in the inner ear of *Srrm4*$^{bv/bv}$ mice, the cerebellum of *Srrm3*$^{gt/gt}$ mice, and the neocortex of dMut mice indicated significant overlaps (Figure 2I). RT-PCR analysis of the splicing of 8 exon targets of SRRM3 and SRRM4 confirmed that their incorporation into mRNA was reduced in the neocortex of dMut mice much more than in the neocortices of the single-gene mutant mice (Figures 2H and S4D). This analysis also revealed that, in the neocortex, SRRM3 and SRRM4 redundantly regulated the alternative splicing of exon 4 of *Rest*. Thus, the molecular functions of SRRM3 and SRRM4 overlap in the neocortex.

SRRM3-SRRM4 Activity Changes GABAergic Neurotransmission from Excitatory to Inhibitory

Our analysis of Gene Ontology annotations of transcripts with splicing defects in dMut mice revealed the lowest p value to be associated with the term “synapse” (Figure 2J). Synapses are critical for the synchronization of neuronal activity. Therefore, we compared the network activity of WT and dMut neurons. Given that dMut mice die during the period of cerebral synaptogenesis, we tested network activity using *in vitro*-differentiated neurons that were derived from the neocortex of WT and dMut mice on E19. Analysis of intracellular Ca^{2+} levels with the Fluo-4 Ca^{2+} indicator demonstrated that similar percentages of WT and dMut neurons exhibited spontaneous Ca^{2+} oscillations on day *in vitro* 8 (DIV8) (Figures S5A and S5B). However, in dMut cultures, the Ca^{2+} oscillations were of an abnormally high amplitude and low frequency and were highly synchronized (Figures 3A, 3F, and S5C–

Author Manuscript Author Manuscript Author Manuscript Author Manuscript

S5G). Thus, the cortical neurons of dMut mice form functional synapses *in vitro*, but their spontaneous activity is abnormal.

The large Ca^{2+} oscillations in dMut neurons are similar to the Ca^{2+} peaks caused by giant depolarizing potentials in the developing brain. These potentials are generated until P5–P7, in part by excitatory GABAergic neurotransmission. At this time, GABA becomes a hyperpolarizing neurotransmitter (Ben-Ari et al., 2007). To test the effect of GABA on Ca^{2+} oscillations, we used the $GABA_AR$ inhibitor gabazine in WT, *Srrm3*$^{gt/gt}$, *Srrm4*$^{bv/bv}$, and dMut cultures. In WT and single-gene mutant cultures, gabazine increased the amplitude and reduced the frequency of Ca^{2+} oscillations (Figures 3A–3E, 3K, S5H, and S5I). In contrast, in dMut cultures, gabazine reduced the amplitude and increased the frequency of Ca^{2+} oscillations (Figures 3F–3K, S5H, and S5I). The negative effect of gabazine on Ca^{2+} peak amplitudes persisted through DIV20 in ~56% of dMut cultures; in the remaining ~44%, it continued beyond this point (Figures 3L and S5J). Thus, SRRM3-SRRM4 activity is necessary for inhibitory GABAergic neurotransmission in cortical neuron cultures.

We used the $GABA_AR$ agonist muscimol to further analyze the abnormal GABA response of dMut neurons. To isolate the effect of muscimol on intracellular Ca^{2+} from spontaneous activity, ionotropic glutamate receptors were blocked with cyanquixaline (CNQX) and MK801. In dMut cortical cell cultures, most neurons responded to muscimol with increased intracellular Ca^{2+} on DIV13 (Figures 3M and 3N). In contrast, in parallel WT cultures, very few neurons responded to muscimol by elevating intracellular Ca^{2+}. Next we used brain slice cultures to retest the difference in the muscimol responses of WT and dMut neurons. Ca^{2+}assays in these cultures confirmed that dMut neurons, but not WT neurons, responded to muscimol with elevated intracellular Ca^{2+} on DIV13 (Figure 3O). We also tested the effect of GABA and the functionally similar neurotransmitter glycine (Gly) in acute spinal cord slices because the spinal cord is the only known CNS region where 40%–60% of neurons are already inhibited by GABA and Gly at birth (Hübner et al., 2001). Fluo-4 assays in acute spinal cord slices revealed that more neurons responded to an equimolar mix of GABA and Gly with elevated intracellular Ca^{2+} in dMut slices than WT slices (Figures 3P and S5K–S5U). Together, these data indicate that SRRM3 and SRRM4 act redundantly to switch the effect of GABA-Gly from excitatory to inhibitory in cortical and spinal cord neurons.

SRRM3-SRRM4 Activity Changes GABAergic Neurotransmission from Excitatory to Inhibitory by Upregulating *Kcc2*

The MJAY analysis of cortical gene expression in WT and dMut mice revealed that *Kcc2* expression was reduced in dMut samples (Table S3). Additionally, qRT-PCR analysis of neocortex, spinal cord, and cortical neuron cultures also demonstrated lower expression of *Kcc2* in dMut samples compared with WT samples (Figure 4A). To test for a potential link between the abnormally low expression of *Kcc2* and the muscimol-evoked Ca^{2+} elevations in dMut neurons, we transfected dMut cortical cell cultures with a KCC2-IRES-tdTomato construct on DIV1 and measured the muscimol-evoked Ca^{2+} responses 7 days later using Fluo-4. dMut neurons that were transfected with KCC2-IRES-tdTomato did not respond to muscimol by increasing intracellular Ca^{2+} whereas those that were untransfected or were

Author Manuscript Author Manuscript Author Manuscript Author Manuscript

transfected with only tdTomato did (Figures 4B–4F). These data suggest that the abnormally low expression of *Kcc2* is a key factor in maintaining the excitatory effect of GABA in dMut cortical neurons.

Our previous and current analyses of the alternative splicing of *Kcc2* demonstrated that incorporation of exon 24 into *Kcc2* is SRRM4-dependent in the inner ear (Nakano et al., 2012) and SRRM3-SRRM4-dependent in the neocortex (Figure S6A). To test whether the incorporation of exon 24 into *Kcc2* affects the function of the encoded protein, we transfected HEK293 cells with either the exon 24-containing or exon 24-omitting splice form of *Kcc2* and measured the cellular uptake of the K^+ analog thallium ion (Tl^+). These assays demonstrated that the presence or absence of exon 24 in the KCC2-IRES-tdTomato construct did not affect KCC2-dependent uptake of Tl^+ by the transfected cells (Figure S6B). Furthermore, transfection of dMut neurons with either splice form of *Kcc2* prevented the excitatory response to muscimol (Figures S6C–S6G). These data indicate that SRRM3-SRRM4-dependent upregulation of *Kcc2*, but not its alternative splicing, is necessary for the GABAergic switch.

SRRM3-SRRM4-Dependent Upregulation of Kcc2 Requires Inactivation of REST

Given that *Kcc2* is a target gene of REST (Karadsheh and Delpire, 2001; ENCODE Project Consortium, 2012), we examined whether other targets of REST were also abnormally repressed in the neocortex of dMut mice. Analysis of the MJAY data revealed that 262 genes were differentially expressed in the neocortex of dMut versus WT mice (Table S3). Among these, 173 were expressed at abnormally low levels. Nearly half (46%) of the 173 genes were orthologs of human genes that had been identified to contain high-confidence REST binding sites in chromatin immunoprecipitation sequencing assays (ENCODE Project Consortium, 2012; Tables S3 and S4; Figure 5A). In contrast, only 4% of all genes expressed in cortical neurons had orthologs of this type (Molyneaux et al., 2015) ($p < 10^{-4}$, χ^2 test). qRT-PCR analysis of a subset of high-confidence target genes of REST confirmed their abnormally low expression in the neocortex of dMut mice (Figure 5B). In contrast, in *Srrm3*$^{gt/gt}$ and *Srrm4*$^{bv/bv}$ mice, the cortical expression of the same genes was not lower than in WT mice (Figure 5B). One of the most downregulated REST target genes in dMut mice encodes the ACTL6B component of the neuronal BAF chromatin modifier complex (Figures 5B and S6H–S6L; Wu et al., 2007), suggesting that SRRM3-SRRM4 alter the composition or amount of the BAF complex in neurons. Together, these gene expression data indicate that SRRM3-SRRM4 activity upregulates cortical expression of multiple target genes of REST.

We used RT-PCR to test the effects of SRRM3 and SRRM4 on the splicing of the frameshift-causing alternative exon of *Rest* (i.e., exon 4) in the neocortex and spinal cord. This analysis demonstrated that the splicing of exon 4 into *Rest* was reduced dramatically in dMut samples relative to WT, *Srrm3*$^{gt/gt}$, and *Srrm4*$^{bv/bv}$ samples (Figures 2H and5C). Likewise, in cortical cell cultures, the dMut genotype (but not the *Srrm3*$^{gt/gt}$ or *Srrm4*$^{bv/bv}$ genotypes) was associated with reduced incorporation of exon 4 into *Rest* (Figures 5C and S6M). Thus, SRRM3 and SRRM4 act redundantly to regulate the splicing of exon 4 of *Rest* in the neocortex and spinal cord.

Author Manuscript Author Manuscript Author Manuscript Author Manuscript

Next we compared the expression levels of *Rest* in the neocortex of WT, *Srrm3*$^{gt/gt}$, *Srrm4*$^{bv/bv}$, and dMut mice. qRT-PCR analysis with primers complementary to exons 2 and 3 of *Rest* revealed that the expression of *Rest* was abnormally high in the neocortex of dMut mice but not in that of the single-gene mutant mice (Figure 5D). Analysis of the MJAY data also suggested higher cortical expression of *Rest* in dMut mice than in WT mice (false discovery rate [FDR]-adjusted p = 0.07). In addition, qRT-PCR analysis of cortical cell cultures demonstrated abnormally high *Rest* expression in dMut samples (Figure 5E). This gene expression defect was not caused by exon 4-dependent differences in nonsense-mediated mRNA decay (NMD) of *Rest* in WT versus dMut neurons because incorporation of exon 4 into *Rest* does not shift the stop codon upstream of the last exon-exon junction (Figure 5C). Thus, SRRM3-SRRM4 activity regulates both the splicing and the expression of *Rest*, but the effect on *Rest* expression is likely indirect.

We tested the potential link between the abnormally high activity of REST and the abnormally low expression of *Kcc2* in dMut neurons. Three-day-old cortical neuron cultures derived from dMut mice were transduced with adeno-associated viruses (AAVs) encoding either a FLAG-tagged dominant-negative fragment of REST (F-dnREST) (Chen et al., 1998) or mCherry (negative control), and *Kcc2* expression was quantified on DIV13 by qRT-PCR. Non-transduced DIV13 cell cultures derived from the neocortex of WT mice served as references. qRT-PCR analysis revealed that *Kcc2* expression was higher in F-dnREST-transduced than mCherry-transduced dMut cultures (Figure 5F), indicating that SRRM3-SRRM4 increase the expression of *Kcc2* by downregulating REST activity.

SRRM3-SRRM4-Dependent Inactivation of REST Regulates the GABAergic Switch

To test the potential link between the abnormally high activity of REST and the preservation of an excitatory GABA effect in dMut neurons, we assessed muscimol-evoked Ca^{2+} changes in F-dnREST-transduced and mCherry-transduced dMut cortical cell cultures on DIV13. Following the Ca^{2+} assays, the expression of F-dnREST was determined in individual cells using anti-FLAG immunostaining. The cells were classified as having low, medium, or high expression of F-dnREST. Only cells with spontaneous Ca^{2+} oscillations were analyzed, i.e., non-neuronal cells were excluded. Comparisons of the muscimol-evoked Ca^{2+} responses in mCherry-expressing neurons versus the three classes of F-dnREST-expressing neurons revealed an association between medium-to-high levels of F-dnREST and reduced responsiveness to muscimol with elevated intracellular Ca^{2+} concentration (Figures 6A–6G). Thus, the abnormally high activity of REST is a key factor in maintaining the immature GABA response of dMut neurons. Together, these data indicate that SRRM3-SRRM4-dependent inactivation of REST regulates the GABAergic switch by de-repressing *Kcc2* (Figure 6H).

DISCUSSION

In the present work, we identify SRRM3 as a neuron-specific splicing factor whose target exons overlap with those of SRRM4. We show that SRRM3 and SRRM4 act redundantly to change GABAergic neurotransmission from excitatory to inhibitory by regulating the REST-dependent repression of *Kcc2* (Figure 6H). Although we cannot rule out the possibility that

Author Manuscript Author Manuscript Author Manuscript Author Manuscript

SRRM3-SRRM4-dependent alterations in the expression or splicing of other mRNAs in addition to *Rest* and *Kcc2* are also necessary for the GABAergic switch, our finding that the excitatory GABA effect can be prevented in dMut neurons by expression of F-dnREST and KCC2 indicates that the SRRM3-SRRM4-REST-KCC2 axis is crucial for regulating the excitatory-to-inhibitory change in GABAergic neurotransmission. Based on the functional similarities between SRRM3 and SRRM4, we suggest that these proteins represent an SRRM sub-family that shares some features with other families of essential splicing factors, such as the NOVA1/NOVA2 and RBFOX1/RBFOX2/RBFOX3 families.

The NOVA and RBFOX proteins are tissue-specific splicing factors that regulate many alternative splicing events in neurons (Vuong et al., 2016). The paralogs within the NOVA, RBFOX, and SRRM3-SRRM4 families have indistinguishable biochemical functions *in vitro*, but in all three families the redundancy *in vivo* is incomplete. Inactivation of any one of the *Rbfox* or *Nova* genes leads to neurological phenotypes in mice, but deletion of either two of the three *Rbfox* genes or of both *Nova* genes, causes perinatal lethality (Raj and Blencowe, 2015; Vuong et al., 2016). The lack of full redundancy in the three families is partly related to spatiotemporal differences in expression of the paralogs (Figures 1F and 2D; Vuong et al., 2016). Nevertheless, some splicing defects are detected even in the *Srrm4*-expressing granular layer of $Srrm3^{gt/gt}$ mice (Figure S3G) and in the *Rbfox1*-expressing neurons of $Rbfox2^{-/-}$ mice (Gehman et al., 2012). This could be due to the amount of remaining paralog being insufficient to support alternative splicing of targets that bind to the splicing factors with low affinity. Alternatively, neuronal expression of paralog-specific interacting proteins may alter the target “preference” of the splicing factors relative to that in non-neuronal heterologous expression systems.

Our data indicate that SRRM3-SRRM4 activity has dual effects on *Rest*: it is necessary for incorporation of exon 4 into *Rest*, and it contributes to downregulation of *Rest* expression. The latter effect is likely indirect because incorporation of exon 4 into *Rest* does not cause NMD of the transcript. Given that more than 70 target genes of REST are expressed at abnormally low levels in the neocortex of dMut mice, the SRRM3-SRRM4-dependent reduction in REST activity is substantial. Notably, these gene expression defects are more severe than those we described for a recently generated mouse line that is heterozygous for an exon 4-deleted dominant allele of *Rest* ($Rest^{+/\Delta Ex4}$) (Nakano et al., 2018). In the neocortex of $Rest^{+/\Delta Ex4}$ mice, only approximately 10 target genes of REST are expressed at abnormally low levels. Furthermore, *Kcc2* expression is not lower in the neocortex of $Rest^{+/\Delta Ex4}$ and $Rest^{\Delta Ex4/\Delta Ex4}$ mice than in that of WT mice on P0 (data not shown). dMut and $Rest^{+/\Delta Ex4}$ mice also differ in the cortical expression of *Rest*; the *Rest* mRNA level is approximately 2.4-fold higher in the neocortex of dMut mice than in that of WT and $Rest^{+/\Delta Ex4}$ mice (Figure S6N). Although the 2.4-fold increase seems modest, a previous study demonstrated that a 2.2-fold increase in *Rest* expression is associated with reduced transcription of several target genes of REST in the neocortex of *Insulinoma 1* knockout mice on E13.5 (Monaghan et al., 2017). Based on these data, we suggest that SRRM3-SRRM4-dependent changes in both the expression and splicing of *Rest* contribute to downregulation of REST activity during neuronal development.

Author Manuscript Author Manuscript Author Manuscript Author Manuscript

Our data reveal that *Srrm3* expression is regulated differently in the neocortex and inner ear. In the inner ear, SRRM4 is critical for the upregulation of *Srrm3*, whereas in the neocortex, SRRM4 is not required for the expression of *Srrm3* (Figure S1B). Thus, the ability of SRRM4 to regulate *Srrm3* expression is tissue-specific. What is the basis for this difference in *Srrm3* regulation between the inner ear and neocortex? We suggest that the answer is related to tissue-specific differences in the regulation of REST, which acts as a transcriptional repressor for *Srrm3* (Lee et al., 2015). In the inner ear, SRRM4 is necessary for the downregulation of REST activity (Nakano et al., 2012). Thus, in this organ, *Srrm3* is upregulated by SRRM4, potentially as a consequence of REST inactivation. In the neocortex, SRRM4 is not essential for the downregulation of REST activity (Figure 5B), and, thus, in this tissue, SRRM4-independent mechanisms may reduce REST activity to levels that are sufficiently low to enable derepression of *Srrm3*. Alternatively, neuron-specific and currently unknown transcriptional activators of *Srrm3* may predominate over REST in regulating *Srrm3* during development. Given that the expression defects of REST target genes are less severe in the neocortex of dMut mice than in the inner ear of $Srrm4^{bv/bv}$ mice (Figure S6O), we favor the model that SRRM3-SRRM4-independent mechanisms of REST inactivation are stronger in the neocortex than the inner ear and that, in the neocortex, they are sufficiently strong to de-repress *Srrm3*. When SRRM3 is expressed, it may maintain the transcription of its own gene by further reducing REST activity.

Our MJAY analysis of dMut mice identified 26 splicing defects that generate or eliminate stop codons at sites over 50 bases upstream of exon-exon junctions (Table S2). In other mRNAs, stop codons at similar positions induce NMD (Popp and Maquat, 2013). Consistent with this phenomenon, 17 of the 26 splicing defects are associated with altered transcript expression in the dMut mouse neocortex (Table S2). These alterations in transcript expression correlate with alterations in the ratio of frame-preserving to frameshifting splice forms; e.g., a higher ratio of frame-preserving to frameshifting splice forms is associated with a higher level of expression for the transcript. These data suggest that SRRM3-SRRM4-dependent splicing of several reading frame-changing exons alters mRNA expression levels, potentially through NMD.

The $Srrm4^{bv/bv}$ genotype is associated with hearing loss and impaired balance, but it does not affect viability. In contrast, a gene trap mutation in *Srrm4* causes partial neonatal lethality characterized by ~10% survival (Quesnel-Vallières et al., 2015). The surviving *Srrm4* gene-trapped pups grow normally and live a normal lifespan but exhibit hearing loss (Bowl et al., 2017), circling, and tremors (Quesnel-Vallières et al., 2015). Histological analysis of *Srrm4* gene-trapped mice (but not $Srrm4^{bv/bv}$ mice) revealed defects in neurite outgrowth, cortical layering, and axon guidance (Quesnel-Vallières et al., 2015). The simplest explanation for the phenotypic differences between the two mouse lines is that the $Srrm4^{bv}$ mutation is hypomorphic, but the gene trap mutation is *null*. Nevertheless, the two mouse lines have important similarities. Neither the alternative splicing of *Rest* nor the expression of REST targets are altered in the CNS of either the $Srrm4^{bv/bv}$ mouse or the *Srrm4* gene-trapped mouse (Figure 5B; Quesnel-Vallières et al., 2015). These data support our model that SRRM4 and SRRM3 act redundantly to regulate REST in the CNS.

Author Manuscript Author Manuscript Author Manuscript Author Manuscript

The cerebellar defects of *Srrm3*$^{gt/gt}$ mice are likely unrelated to the KCC2-dependent regulation of GABAergic neurotransmission because cerebellum-specific deletion of *Kcc2* does not cause overt motor deficits in mice (Seja et al., 2012). Furthermore, our MJAY analysis of cerebellar RNA samples did not reveal any difference in *Kcc2* expression between WT and *Srrm3*$^{gt/gt}$ mice. However, SRRM3 does regulate the alternative splicing of 17 transcripts that have been shown to encode critical proteins for cerebellar function (Table S1). Further studies are required to determine whether these splicing changes contribute to the cerebellar pathology in *Srrm3*$^{gt/gt}$ mice.

SRRM4 expression is frequently reduced in the brain of human subjects diagnosed with autism spectrum disorder (Irimia et al., 2014). In mice, heterozygosity for the *Srrm4* gene trap allele causes abnormally low expression of the SRRM4 protein, impaired synaptic transmission in the somatosensory cortex, and autism-like behavior (Quesnel-Vallières et al., 2016). Thus, in humans, heterozygosity for *SRRM4*-inactivating mutations is a potential risk factor for autism spectrum disorder. In contrast, heterozygosity for *SRRM3*-inactivating mutations has not been proposed to cause any disease.

Our data demonstrate that SRRM3 and SRRM4 regulate the alternative splicing of overlapping groups of exons in the brain. A very recent study also identified a number of common exon targets of SRRM3 and SRRM4 using small interfering RNA (siRNA)-mediated knockdown of the two proteins in the N2A cell line (Gonatopoulos-Pournatzis et al., 2018). In addition, SRRM3-SRRM4 activity regulates the expression level of a large number of transcripts in the nervous system (Table S3). Depending on the extent to which SRRM3-SRRM4 activity is reduced, the cellular and functional consequences in mice include impaired synaptic transmission in the somatosensory cortex, loss of hair cells, degeneration of Purkinje cells, or preservation of excitatory GABAergic neurotransmission. Establishing which SRRM3-SRRM4-regulated exons are etiologically related to each defect is critical for understanding the role of alternative splicing in neuronal function and development.

STAR⋆METHODS

CONTACT FOR REAGENTS AND RESOURCE SHARING

Further information and requests for resources and reagents should be directed to and will be fulfilled by the Lead Contact, Botond Banfi (botond-banfi@uiowa.edu).

EXPERIMENTAL MODEL AND SUBJECT DETAILS

Mice—All mouse procedures were approved by the University of Iowa Institutional Animal Care and Use Committee. Mice were housed in groups in temperature-controlled rooms (21 ± 2°C) with a 12 h/12 h light/dark cycle. Food and water were available for the mice *ad libitum*. Animal husbandry and health status monitoring were provided by the Office of Animal Resources staff at the University of Iowa. The ages of tested mice are indicated in the figure legends. The sexes of pre-weaned mice were not determined. The sexes of weaned mice (P21 and older) were documented. *Srrm3*$^{+/gt}$ mice were generated using the C57BL/6 ES cell clone IST12726F8 at the Texas A&M Institute for Genomic Medicine. Litters of

Author Manuscript Author Manuscript Author Manuscript Author Manuscript

Srrm3$^{+/gt}$ breeding pairs and *Srrm3*$^{+/gt}$;*Srrm4*$^{bv/bv}$ breeding pairs were genotyped using tail DNA and conventional PCR (see primers in Table S5). Male and female *Srrm3*$^{gt/gt}$ mice exhibited equally severe phenotypes. The *Srrm4*$^{bv/bv}$ and *Rest*$^{+/\Delta Ex4}$ mouse lines and their genotyping were described previously (Nakano et al., 2012, 2018).

Cell Lines, Cortical Cell Culture, and Brain Slice Culture—HEK293 cells (female), N2A cells (male), NIH 3T3 cells (male), and mIMCD-3 cells (sex not known) were obtained from the American Type Culture Collection (ATCC). HEK293 cells and mIMCD-3 cells were grown in Dulbecco's Modified Eagle Medium/Nutrient Mixture F-12 (DMEM/F-12; Corning). N2A cells and NIH 3T3 cells were grown in DMEM (Corning). Both DMEM/F12 and DMEM were supplemented with 10% fetal bovine serum (FBS; Atlanta Biologicals), penicillin (100 units/mL; Thermo Fisher Scientific), and streptomycin (100 μg/mL; Thermo Fisher Scientific). To generate primary cultures of cortical neurons, the neocortex of E19 mice was dissected from the brain and dissociated into a single cell suspension using the Papain Dissociation System (Worthington Biochemical Corporation) following the manufacturer's instructions. The sexes of these mice were not determined. The dissociated cortical cells were resuspended in Neurobasal-A culture medium (Thermo Fisher Scientific) supplemented with B-27 Supplement (Thermo Fisher Scientific), L-glutamine (2 mM; Thermo Fisher Scientific), penicillin (100 units/mL; Thermo Fisher Scientific), and streptomycin (100 μg/mL; Thermo Fisher Scientific). The cells were plated onto poly-D-lysine-coated coverslips (12 mm in diameter) at a density of 5–10 × 10^5 cells per coverslip. Half of the culture medium was exchanged for fresh medium every 3 days. All cell cultures were incubated at 37°C in a humidified air atmosphere containing 5% CO_2 until use.

To generate brain slice cultures, brain was dissected from E19 WT and dMut mice in ice-cold Slice Buffer (92 mM NaCl, 2.5 mM KCl, 1.2 mM NaH_2PO_4, 30 mM $NaHCO_3$, 20 mM HEPES, 25 mM glucose, 10 mM $MgSO_4$, 0.5 mM $CaCl_2$, 3 mM sodium pyruvate, 2 mM thiourea, 5 mM sodium ascorbate, pH 7.4), embedded into low-melt agarose gel (5%), and sliced into 250 μm thick sections using a Compresstome VF-200 Vibrating Microtome (Precisionary Instruments). The Compresstome buffer tray was filled with ice-cold Slice Buffer. Just prior to use, Slice Buffer was bubbled with O_2/CO_2 mixed gas (95% O_2 and 5% CO_2) for 45–60 min to increase its O_2 content. Brain slices were transferred from the buffer tray onto transwell inserts in 6-well plates (Corning). The tissue culture medium for slice cultures consisted of 25% horse serum (Thermo Fisher Scientific), 25% HBSS (Thermo Fisher Scientific), 50% Basal Medium Eagle (Thermo Fisher Scientific) supplemented with L-glutamine (1 mM; Thermo Fisher Scientific), penicillin (100 units/mL; Thermo Fisher Scientific), streptomycin (100 μg/mL; Thermo Fisher Scientific), glucose (27.5 mM; Sigma), and pyruvate (5 mM; Sigma). This culture medium was added only to the lower chamber to create an air-liquid interface at the upper surface of the trans-well insert. Brain slice cultures were incubated at 37°C in a humidified air atmosphere containing 5% CO_2 until use. From DIV2, the culture medium was supplemented with cytarabine, 5-fluoro-2′-deoxyuridine, and uridine (1.67 μM each; Sigma) to moderate glial cell growth. Half of the culture medium was exchanged for fresh medium every 2 days.

Author Manuscript Author Manuscript Author Manuscript Author Manuscript

METHOD DETAILS

Rotarod and Motor Dysfunction Tests—For rotarod test, mice were placed onto a cylinder rotating at fixed speed (10 rpm), and latency to fall was measured for a maximum of 180 s. Each mouse was tested 4 times. The latency to fall was measured in the 2nd, 3rd, and 4th trials. The longest time the mouse could spend on the rotating rod during these trials was used for statistical analysis (Figure S2D).

To calculate the motor dysfunction score, 3 subscores were determined and summed (Guyenet et al., 2010). These subscores quantify motor coordination and muscle tone based on ledge-test performance, gait, and kyphosis. The 3 subscores (each ranging from 0–3, with 0 meaning no deficiency) were determined by an observer blinded to the genotypes of the mice being tested.

For the ledge-test, mice were placed on the ledge of the cage and movement was scored. If the mouse walked along the ledge of the cage or lowered itself into the cage without losing balance, it received a score of 0. If it lost footing while walking along the edge but otherwise appeared coordinated, it received a score of 1. If it did not use its hind legs effectively or landed on its head while descending into the cage, it received a score of 2. If it fell off the ledge or refused to walk along the ledge, it received a score of 3.

Gait was evaluated on a flat surface. A score of 0 was given if the mouse moved normally without its belly touching the ground. If the mouse had tremor or limped, it received a score of 1. If it had severe tremor, a severe limp, a lowered pelvis, or feet pointed away from the body, it received a score of 2. If it had difficulty moving forward or could not lift the abdomen from the ground, it received a score of 3.

Kyphosis (a sign of reduced muscle tone) was also evaluated on a flat surface during walking. If the mouse was able to straighten its spine easily during walking and did not have persistent kyphosis, it received a score of 0. If it had mild kyphosis but could straighten its spine during walking, it received a score of 1. If it could not straighten its spine during walking but the kyphosis was mild, it received a score of 2. If it had pronounced and sustained kyphosis as it walked or sat, it received a score of 3.

Laser-Capture Microdissection—Cerebellum was dissected from WT and *Srrm3*$^{gt/gt}$ mice on P16 and embedded into Tissue Freezing Medium (General Data Healthcare, Inc.) without cryoprotection or fixation. The embedded tissue was frozen in liquid nitrogen, cryosectioned, and stored at −80°C. Just before laser capture microdissection, the slides were incubated in the following series of solutions at room temperature: 95% ethanol (45 s), 75% ethanol (30 s), 50% ethanol (30 s), water (30 s), water (second jar, 30 s), 50% ethanol (30 s), 75% ethanol (30 s), 95% ethanol (30 s), 100% ethanol (60 s), 100% ethanol (second jar, 120 s), xyelene (90 s), and xylene (second jar, 240 s). Water and the 75% and 50% ethanol solutions contained an RNase inhibitor (0.2% volume, ProtectRNA; Sigma). Finally, sections were air-dried for several minutes before laser capture microdissection with a Pixcell II instrument (Arcturus Engineering Inc.). RNA was isolated from the captured tissue using the Arcturus PicoPure Frozen RNA Isolation Kit (Thermo Fisher Scientific).

Author Manuscript Author Manuscript Author Manuscript Author Manuscript

Isolation and RT-PCR Analysis of RNA—For the isolation of cortical and cerebellar RNA, the neocortex and cerebellum were dissected from the brain and homogenized in Trizol Reagent (Thermo Fisher Scientific). RNA was extracted from the homogenized tissue with chloroform and precipitated with isopropanol. RNA was then dissolved in water, incubated with DNase, and further purified on the separation column from an RNeasy Mini Kit (QIAGEN) following the manufacturer's instructions. For the isolation of utricular RNA, utricular macula was dissected from the inner ear. RNA was isolated from 4–8 pooled utricular maculas using the RNeasy Micro Kit (QIAGEN). RNA was isolated from primary cell cultures and cell lines using the RNeasy Mini Kit (QIAGEN). RNA samples were reverse transcribed using SuperScript III reverse transcriptase (Thermo Fisher Scientific). The cDNA samples were analyzed using the HotStarTaq PCR kit (QIAGEN) or the qPCR kit PerfeCTa SYBR Green FastMix (Quantabio). PCR and qPCR primers are shown in Table S5. PCR products less than 200 bp in length were separated in polyacrylamide gels; larger PCR products were separated in agarose gels.

Analyses of Microarray Data and GO Annotations—RNA samples from 4 mice per genotype were used for microarray analyses. RNA samples were processed using the NuGEN WT-Ovation Pico RNA Amplification System, NuGEN WT-Ovation Exon Module, and NuGEN FL-Ovation cDNA Biotin Module. The cDNA probes were hybridized to microarrays (MJAYs, Affymetrix Inc.), and the arrays were subsequently scanned using an Affymetrix Model 3000 scanner with 7G upgrade. Data were collected using GeneChip Operating Software. Raw microarray CEL files were imported into the Partek Genomics Suite 6.6 (Partek, Inc.). Signal intensities for the probe sets were quantile normalized and median polished using Robust Multichip Average background correction. Probe set signals were summarized to genes to calculate the overall level of expression for each gene represented in the MJAY, and the difference in expression (Δexp) was calculated for each detected gene in mutant (i.e., *Srrm3*$^{gt/gt}$ and dMut) versus WT samples. Adjusted probe-set intensities (*I*ProbeAdj) were calculated for the mutant (M) datasets by adjusting the signal intensity for each probe set (*I*ProbeM) with Δexp of the corresponding gene (*I*ProbeAdjM = *I*ProbeM – Δexp). This approach produced fewer false positive hits than did normalization based on dividing the background-corrected signal intensities of exon and exon-junction probe sets by background-corrected signal for the corresponding gene. *I*ProbeAdjM was compared to the signal intensity of the corresponding probe set in WT samples (*I*ProbeWT). To maximize the discovery rate for signal differences, *I*ProbeAdjM and *I*ProbeWT were analyzed by two-tailed Student's t test. Extensive post-statistical filtering and RT-PCR testing were used to compensate for the high rate of type I error associated with the use of Student's t test in multiple comparisons. Probe sets with significant differences between *I*ProbeAdjM and *I*ProbeWT ($p < 0.01$) were queried against the Affymetrix annotation map file (which contains alternative/constitutive annotations for each measured splicing event), and probe sets that measured constitutive events were filtered out. The remaining probe sets were queried against the SIB Alt-Splicing track in the UCSC Genome Browser to identify and eliminate those that either showed greater than 50% identity with more than one gene or measured alternative promoter activity. The sequences of the remaining probe sets were queried against the mouse genome to identify those that measured the same alternative splicing events. We required that probe sets targeting competing isoforms had opposing

Author Manuscript Author Manuscript Author Manuscript Author Manuscript

trends in the change in signal intensity (Shen et al., 2010). In the first round of analysis, the frequency of an alternative splicing event was considered to differ significantly between the control and test groups if the difference in normalized intensities for at least 2 probe sets per splicing event resulted in p values of less than 0.01. Because ~84% of the identified changes in splicing affected exons that were expressed only in neural tissues (based on EST evidence), in the second round of analysis we used 'neural tissue-specific splicing' as a new criterion for scrutinizing the list of exons for which a single probe set suggested abnormal splicing ($p < 0.01$) in the *Srrm3*$^{gt/gt}$ or dMut group. This approach did not increase the false positive rate (based on verification by RT-PCR), but nearly doubled the number of exons identified as differentially spliced in the mutant versus WT group. If differences in the signal intensities of more than one probe set indicated a splicing difference for a single exon in mutant versus WT groups, the splicing difference-indicating probe set signals were averaged for the exon (Figures 2B and 2G; Tables S1 and S2). Our microarray datasets have been deposited in the Gene Expression Omnibus under accession number GEO: GSE71481.

To identify the REST targets among the genes differentially expressed in WT and dMut mice, we created a list of REST-binding genes based on genome-wide REST ChIP-seq data from ENCODE (ENCODE Project Consortium, 2012). A given REST ChIP-seq peak from ENCODE was considered indicative of REST binding if the associated Cluster Score was higher than 700 in the 'wgEncodeRegTfbsClusteredV2' table of the UCSC Table Browser (Karolchik et al., 2004). Even high score peaks were filtered out if the peaks were not located within a RefSeq-annotated gene or maximum 6 kb upstream of the transcription start site of a gene. The ENCODE ChIP-seq dataset was generated using human cell lines (ENCODE Project Consortium, 2012). We refer to the mouse orthologs of these human REST-binding genes as 'high-confidence REST targets' (Table S4).

GO annotations of differentially expressed genes were identified and analyzed using the DAVID software (Huang et al., 2009). All genes represented on MJAY were used as the background gene set for the GO annotation analysis. Enrichment p values for GO annotations were calculated in DAVID using Fisher's exact test and the Benjamini-Hochberg correction procedure for multiple testing.

LacZ Tissue Staining, Histochemistry, and Immunostaining—LacZ activity in the brains of P0 and P16 mice was detected using the LacZ Tissue Staining Kit (InvivoGen) according to the manufacturer's instructions. For histochemical analysis, brains and lungs from E19 mice were fixed with 4% paraformaldehyde (PFA) in PBS for 2 days at 4°C. Older mice were transcardially perfused with 4% PFA in PBS while under deep anesthesia. Brains and lungs were embedded in paraffin, sectioned, and stained with cresyl violet or hematoxylin and eosin. For immunostaining, PFA-fixed brains were cryoprotected, embedded into Tissue Freezing Medium (General Data Healthcare, Inc.), and cryosectioned. The sections were probed with an anti-calbindin D-28K antibody (1:100 dilution of CB-955 monoclonal antibody or 1:1,000 dilution of a rabbit polyclonal antibody, see antibodies in Key Resources Table), an anti-neurofilament antibody (1:900 dilution), or a rabbit anti-Ki67 antibody (1:100 dilution). The secondary antibodies were Alexa 488-conjugated anti-mouse antibody (1:300 dilution) and Alexa 594-conjugated anti-rabbit antibody (1:300 dilution). The expression of MAP2 and F-dnREST in cortical cell cultures was visualized using an

Author Manuscript Author Manuscript Author Manuscript Author Manuscript

anti-MAP2 antibody (1:900 dilution), an anti-FLAG antibody (1:200 dilution), and Alexa 594-conjugated secondary antibodies (1:300 dilution). Total cell numbers in the imaged areas of coverslips were determined using Topro-3 nuclear stain (Thermo Fisher Scientific). Images of immunostained samples were obtained using a confocal microscope (LSM-510, Carl Zeiss Inc.). Images of histochemically stained samples were obtained using an Eclipse TE2000-U microscope (Nikon) and a DS-Fi2 camera (Nikon).

***In Situ* Hybridization—**Mice were transcardially perfused with 4% PFA in PBS while under deep anesthesia. Selected regions of the central nervous system were dissected, fixed with 4% PFA in PBS for an additional 16 h, embedded into Tissue Freezing Medium (General Data Healthcare, Inc.), and cryosectioned. Type-1 probes specific for *Srrm3* and *Srrm4* and type-6 probes specific for *Rbfox3* were designed and synthesized at Affymetrix. The transcript-specific probes and secondary (pre-amplifier and amplifier) probes were hybridized to cryosections using the ViewRNA ISH Tissue 2-Plex Assay Kit (Affymetrix) according to the manufacturer's instructions. Hybridized sections were counterstained with Gill's hematoxylin for light microscopy, and with Sytox blue for fluorescence microscopy.

Scoring of In Situ Hybridization Images from the Allen Brain Atlas—Brain *in situ* hybridization images of transcripts differentially spliced in the inner ear of WT and *Srrm4*$^{bv/bv}$ mice were downloaded from the Allen Brain Atlas (Lein et al., 2007; Nakano et al., 2012). The downloaded images were scored for the distribution of *in situ* hybridization signals by a team member (B.B.) blinded to the identity of analyzed transcripts. Transcripts were scored '0' if the *in situ* hybridization signal was weaker in the Purkinje cell layer than in the molecular or granular layer. Transcripts were scored '1' if the *in situ* hybridization signal was equally strong in the Purkinje cell layer versus the molecular or granular layer. Transcripts were scored '2' if the *in situ* hybridization signal was stronger in the Purkinje cell layer than in the molecular and granular layers.

Immunoblotting—The nuclear protein fraction was isolated from the isocortex of E19 mice using the Nuclear Complex Co-IP Kit (Active Motif) according to the manufacturer's instructions. The nuclear protein fraction was resolved by SDS polyacrylamide gel electrophoresis, electroblotted onto a nitrocellulose membrane, and probed using a monoclonal anti-ACTL6B antibody (1:6 dilution, see antibodies in Key Resources Table) and rabbit anti-LMNB1 antibody (1:5,000 dilution). The signal was detected using an HRP-conjugated anti-mouse antibody (1:10,000 dilution) or an HRP-conjugated anti-rabbit antibody (1:10,000 dilution) and SuperSignal West Pico Chemiluminescent Substrate (Thermo Fisher Scientific).

Minigene Assays—Alternative exons and adjacent ~800 bp intronic sequences were PCR amplified (see primers in Table S5) and subcloned into the exon trap pET-01 vector (Mobitec). Mutated versions of the minigenes were generated using overlap-extension PCR. HEK293 cells were co-transfected (using Lipofectamine LTX from Invitrogen) with these minigenes plus either an empty expression vector or one that encodes SRRM4, SRRM3, or SRSF1 (Addgene plasmid 17990, (Phair and Misteli, 2000)). 24 h after transfection, RNA was isolated from the transfected cell cultures and analyzed by RT-PCR as described in the

Author Manuscript Author Manuscript Author Manuscript Author Manuscript

'Isolation and RT-PCR Analysis of RNA' section. The primers for the RT-PCR analysis are shown in Table S5.

Luciferase Assays—The predicted mouse *Actl6b* promoter region (chr5:137,553,163–137,553,637 in GRCm38/mm10 assembly) was inserted into the pGL4.10 vector (Promega). Site-directed mutagenesis of the RE1 motif in the *Actl6b* promoter was carried out using overlap-extension PCR. WT or a mutant version of the *Actl6b*-pGL4.10 construct was mixed with the pGL4.7Rluc vector and used to co-transfect N2A and HEK293 cells, along with plasmids encoding REST (Nakano et al., 2018), REST4 (Nakano et al., 2018), F-dnREST, SRRM3, SRRM4, or no insert. 36 h after transfection, luciferase activities were measured using the Dual-Luciferase Reporter Assay System (Promega).

AAV Production—AAV1 with a CAG-F-dnREST expression cassette was prepared by the Gene Vector Core facility at the University of Iowa using the triple transfection method (Yang et al., 2002). AAV1 with a CAG-Cre-mCherry expression cassette was purchased from SignaGen Laboratories.

Spinal Cord Slice Preparation—To generate acute spinal cord slices, spinal cords were dissected from E19 WT and dMut mice in ice-cold Slice Buffer (described in the 'Cell Lines, Cortical Cell Culture, and Brain Slice Culture' section), embedded into low-melt agarose gel (5%), and sliced into 250 μm thick sections using a Compresstome VF-200 Vibrating Microtome (Precisionary Instruments). The Compresstome buffer tray was filled with ice-cold Slice Buffer that was oxygenated using a gas mix of O_2 (95%) and CO_2 (5%). Slices were kept in Slice Buffer at RT for 1 hour after sectioning to facilitate cell recovery. Between recovery and the Ca^{2+} assay (for a maximum of 3 h), slices were incubated in oxygenated BrainPhys cell culture medium (StemCell Technologies) supplemented with glucose (25 mM; Sigma) and sodium pyruvate (4.5 mM; Sigma).

Calcium Imaging—Primary cultures of cortical neurons were generated as described in the 'Cell Lines, Cortical Cell Culture, and Brain Slice Culture' section. Cells were loaded with Fluo-4 AM (5 μg/mL; Thermo Fisher Scientific) in the presence of Pluronic-F27 (0.01%; Thermo Fisher Scientific) in BrainPhys medium (StemCell Technologies) at 37°C for 10 min. The loading medium was replaced with Fluo-4 AM-free BrainPhys, and cells were incubated for an additional 10 min before imaging. Fluorescence signals were recorded at a rate of 5Hz with an Eclipse TE2000U microscope (Nikon) fitted with a Cool-Snap camera (1,392 × 1,040 pixels; Photometrix), a heating stage (37°C), and a fluorescence light source. Synchronization of spontaneous neuronal activity was quantified in the recordings using the automatic peak recognition ($\Delta F/F_0 > 10\%$) function of the FluoroSNNAP software (Patel et al., 2015). The amplitude and frequency of fluorescence peaks were analyzed manually in ImageJ and MATLAB, using $\Delta F/F_0 > 2\%$ as a cut-off and morphological features (rapid rise and slower decay) for peak recognition. Only the somata of cells were selected for analysis. Chicken β-actin promoter (CAG)-F-dnREST and CAG-Cre-mCherry (control) expression cassettes were delivered to the cultures using AAV1 (2.5×10^{11} viral genome/12 mm coverslip). To express KCC2 and tdTomato in neurons, cortical cell cultures were transfected with CAG-KCC2-IRES-tdTomato (Addgene 61404, (Bortone and Polleux,

Author Manuscript Author Manuscript Author Manuscript Author Manuscript

2009)), CAG-KCC2^{Ex24-}-IRES-tdTomato, or CAG-tdTomato plasmids using the Lipofectamine 3000 reagent. Brain slice cultures and acute spinal cord slices were prepared as described in the 'Cell Lines, Cortical Cell Culture, and Brain Slice Culture' and 'Spinal Cord Slice Preparation' sections. Slice cultures and acute slices were loaded with Fluo-4 AM (5 μg/mL; Thermo Fisher Scientific) in the presence of Pluronic-F27 (0.01%; Thermo Fisher Scientific) in BrainPhys medium (StemCell Technologies) at 37°C for 45 min. The loading medium was replaced with Fluo-4 AM-free BrainPhys twice, and slices were incubated for an additional 15 min before imaging. Ligand-gated ion channel agonists and antagonists were used at the following concentrations (in μM): gabazine 2, CNQX 25, MK801 25, muscimol 5, GABA 25, and Gly 25.

Tl^+ Uptake Assay in HEK293 Cell Cultures—HEK293 cells were transfected with pCITF vector containing CAG-KCC2-IRES-tdTomato, CAG-KCC2^{Ex24-}-IRES-tdTomato, or CAG-tdTomato expression cassettes using Lipofectamine LTX and PLUS Reagent (Thermo Fisher Scientific). 24 h after transfection, Tl^+ uptake by HEK293 cells was quantified using the FluxOR II Green Potassium Ion Channel Assay (Thermo Fisher Scientific) according to the manufacturer-provided 'Wash Method'. The Tl^+ uptake assay was started by adding Tl^+ (2 mM final concentration) to the cell culture medium (DMEM/F-12). Green fluorescence was recorded for 30 s before and 120 s immediately after starting the assay using an Eclipse TE2000U microscope (Nikon) fitted with a Cool-Snap camera (Photometrix), a heating stage (37°C), and a fluorescence light source. At the end of the assay, red fluorescence in the imaged field was recorded for the identification of transfected cells. The change in FluxOR II fluorescence in the first 30 s immediately after adding Tl^+ to the culture medium was analyzed using ImageJ.

QUANTIFICATION AND STATISTICAL ANALYSIS

Data are presented as individual data points or mean ± standard error of the mean (SEM), as indicated in the corresponding figure legends. The statistical methods applied are either indicated in the figure legend or described in the main text. Sample sizes were not determined *a priori*. Microarray data and GO annotations were analyzed using the Partek Genomics Suite and the DAVID bioinformatics tool, respectively (see 'Analysis of Microarray Data and GO Annotations' section). All other data analyses were performed with GraphPad Prism version 7. For the datasets analyzed using GraphPad Prism, assumptions of normality were tested with the Shapiro-Wilk test and assumptions of equal variance were determined with either the F-test (for two groups) or the Brown-Forsythe test (for three or more groups).

In cases where assumptions of normality and equal variance were not violated, parametric tests were used for the further analysis of datasets: the one-sample t test was used to compare the mean of one group to a hypothetical value; the unpaired Student's t test was used to compare the means of two groups; and one-way ANOVA was used to compare the means of three or more groups. When ANOVA revealed significant findings, Dunnett's or Tukey's post hoc test was used. Dunnett's test was selected when the means of test groups were compared to the mean of a control group, and Tukey's test was selected when all possible pairs of means were compared.

Author Manuscript Author Manuscript Author Manuscript Author Manuscript

In the few cases where the assumption of equal variance (but not normality) was violated, Welch's t test was used to compare the means of two groups.

In cases where the assumption of normality (but not equal variance) was violated, non-parametric tests were used: the Mann-Whitney test was used to compare the medians of two groups; and the Kruskal-Wallis test was used to determine whether one sample stochastically dominates another sample in a group of three or more samples. When the Kruskal-Wallis test revealed significant findings, Dunn's post hoc test was used to compare the test groups with a control group.

In cases where assumptions of both normality and equal variance were violated, one of two approaches was selected.

- Datasets presented in Figures 3L, 3N, 6G, and S5C were log2 transformed. Given that some of the data in Figures 3N and 6G are negative numbers, a fixed number was added to each data point (0.86 in Figure 3N and 0.19 in Figure 6G) prior to log2 transformation. Statistical tests for the transformed data were selected based on results from the Shapiro-Wilk test and homogeneity of variance tests (F-test for two groups and Brown-Forsythe test for three or more groups). Specifically, when assumptions of normality (but not equal variance) were violated by the transformed data, the Mann-Whitney or Kruskal-Wallis test was selected, depending on the number of compared groups (Figures 3N, 6G, and S5C); when assumptions of normality and equal variance were not violated by the transformed data, unpaired Student's t test with FDR correction was used (Figure 3L).
- Datasets presented in Figures 3O, 3P, S2D, S2E, and S3E were analyzed using a parametric test (i.e., Welch's t test with or without FDR correction, depending on the number of compared groups) on non-transformed data. In these figures, ceiling and floor effects led to violations of normality and equal variance assumptions. In the context of these figures, ceiling and floor effects increase the probability of type II error (false negative) but not type I error (false positive).

In figure panels where multiple one-sample tests or two-group tests were used, the Benjamini-Hochberg procedure was applied to limit the false discovery rate (FDR) at 0.05, as indicated in the relevant figure legends. The statistical significance of 3-group overlaps (Figure 2J) was calculated using the Monte Carlo method in R. $p < 0.05$ is considered statistically significant unless otherwise specified. Numbers of animals and biological replicates of assays (n) are reported in the figure legends if a statistical test was used or if individual data points are not shown in the corresponding figure.

DATA AND SOFTWARE AVAILABILITY

The accession number for the microarray data reported in this paper is GEO: GSE71481.

Supplementary Material

Refer to Web version on PubMed Central for supplementary material.

Author Manuscript Author Manuscript Author Manuscript Author Manuscript

ACKNOWLEDGMENTS

We thank Dr. Tom Misteli (National Cancer Institute, Bethesda, MD) for providing the SRSF1-encoding plasmid, Dr. Stephen Elledge (Harvard Medical School, Boston, MA) for providing the REST-encoding plasmid, Dr. Franck Polleux (Columbia University Medical Center, New York, NY) for providing the KCC2-tdTomato-encoding plasmid, and Drs. Christine Blaumueller and Jennifer Y. Barr (University of Iowa) for critical review of the manuscript. The microarray data presented herein were obtained at the Genomics Division of the Iowa Institute of Human Genetics, which is supported in part by the University of Iowa Carver College of Medicine. This project was supported by grants from the NIDCD/NIH (R01DC010152 and R01DC014953 to B.B.).

REFERENCES

Ballas N, Grunseich C, Lu DD, Speh JC, and Mandel G (2005). REST and its corepressors mediate plasticity of neuronal gene chromatin throughout neurogenesis. Cell 121, 645–657. [PubMed: 15907476]

Ben-Ari Y, Gaiarsa JL, Tyzio R, and Khazipov R (2007). GABA: a pioneer transmitter that excites immature neurons and generates primitive oscillations. Physiol. Rev 87, 1215–1284. [PubMed: 17928584]

Bortone D, and Polleux F (2009). KCC2 expression promotes the termination of cortical interneuron migration in a voltage-sensitive calcium-dependent manner. Neuron 62, 53–71. [PubMed: 19376067]

Bowl MR, Simon MM, Ingham NJ, Greenaway S, Santos L, Cater H, Taylor S, Mason J, Kurbatova N, Pearson S, et al.; International Mouse Phenotyping Consortium (2017). A large scale hearing loss screen reveals an extensive unexplored genetic landscape for auditory dysfunction. Nat. Commun 8, 886. [PubMed: 29026089]

Bruce AW, Donaldson IJ, Wood IC, Yerbury SA, Sadowski MI, Chapman M, Göttgens B, and Buckley NJ (2004). Genome-wide analysis of repressor element 1 silencing transcription factor/neuron-restrictive silencing factor (REST/NRSF) target genes. Proc. Natl. Acad. Sci. USA 101, 10458–10463. [PubMed: 15240883]

Chen ZF, Paquette AJ, and Anderson DJ (1998). NRSF/REST is required in vivo for repression of multiple neuronal target genes during embryogenesis. Nat. Genet 20, 136–142. [PubMed: 9771705]

ENCODE Project Consortium (2012). An integrated encyclopedia of DNA elements in the human genome. Nature 489, 57–74. [PubMed: 22955616]

Gehman LT, Meera P, Stoilov P, Shiue L, O'Brien JE, Meisler MH, Ares M Jr., Otis TS, and Black DL (2012). The splicing regulator Rbfox2 is required for both cerebellar development and mature motor function. Genes Dev 26, 445–460. [PubMed: 22357600]

Gonatopoulos-Pournatzis T, Wu M, Braunschweig U, Roth J, Han H, Best AJ, Raj B, Aregger M, O'Hanlon D, Ellis JD, et al. (2018). Genome-wide CRISPR-Cas9 Interrogation of Splicing Networks Reveals a Mechanism for Recognition of Autism-Misregulated Neuronal Microexons. Mol. Cell 72, 510–524.e2. [PubMed: 30388412]

Guyenet SJ, Furrer SA, Damian VM, Baughan TD, La Spada AR, and Garden GA (2010). A simple composite phenotype scoring system for evaluating mouse models of cerebellar ataxia. J. Vis. Exp 39, 1787.

Huang W, Sherman BT, and Lempicki RA (2009). Systematic and integrative analysis of large gene lists using DAVID bioinformatics resources. Nat. Protoc 4, 44–57. [PubMed: 19131956]

Hübner CA, Stein V, Hermans-Borgmeyer I, Meyer T, Ballanyi K, and Jentsch TJ (2001). Disruption of KCC2 reveals an essential role of K-Cl cotransport already in early synaptic inhibition. Neuron 30, 515–524. [PubMed: 11395011]

Irimia M, Weatheritt RJ, Ellis JD, Parikshak NN, Gonatopoulos-Pournatzis T, Babor M, Quesnel-Vallières M, Tapial J, Raj B, O'Hanlon D, et al. (2014). A highly conserved program of neuronal microexons is misregulated in autistic brains. Cell 159, 1511–1523. [PubMed: 25525873]

Karadsheh MF, and Delpire E (2001). Neuronal restrictive silencing element is found in the KCC2 gene: molecular basis for KCC2-specific expression in neurons. J. Neurophysiol 85, 995–997. [PubMed: 11160529]

Author Manuscript Author Manuscript Author Manuscript Author Manuscript

Karolchik D, Hinrichs AS, Furey TS, Roskin KM, Sugnet CW, Haussler D, and Kent WJ (2004). The UCSC Table Browser data retrieval tool. Nucleic Acids Res 32, D493–D496. [PubMed: 14681465]

Lee NS, Evgrafov OV, Souaiaia T, Bonyad A, Herstein J, Lee JY, Kim J, Ning Y, Sixto M, Weitz AC, et al. (2015). Non-coding RNAs derived from an alternatively spliced REST transcript (REST-003) regulate breast cancer invasiveness. Sci. Rep 5, 11207. [PubMed: 26053433]

Lein ES, Hawrylycz MJ, Ao N, Ayres M, Bensinger A, Bernard A, Boe AF, Boguski MS, Brockway KS, Byrnes EJ, et al. (2007). Genome-wide atlas of gene expression in the adult mouse brain. Nature 445, 168–176. [PubMed: 17151600]

Li Y, Donmez N, Sahinalp C, Xie N, Wang Y, Xue H, Mo F, Beltran H, Gleave M, Wang Y, et al. (2017). SRRM4 Drives Neuroendocrine Transdifferentiation of Prostate Adenocarcinoma Under Androgen Receptor Pathway Inhibition. Eur. Urol 71, 68–78. [PubMed: 27180064]

Molyneaux BJ, Goff LA, Brettler AC, Chen HH, Hrvatin S, Rinn JL, and Arlotta P (2015). DeCoN: genome-wide analysis of in vivo transcriptional dynamics during pyramidal neuron fate selection in neocortex. Neuron 85, 275–288. [PubMed: 25556833]

Monaghan CE, Nechiporuk T, Jeng S, McWeeney SK, Wang J, Rose-nfeld MG, and Mandel G (2017). REST corepressors RCOR1 and RCOR2 and the repressor INSM1 regulate the proliferation-differentiation balance in the developing brain. Proc. Natl. Acad. Sci. USA 114, E406–E415. [PubMed: 28049845]

Moore YE, Kelley MR, Brandon NJ, Deeb TZ, and Moss SJ (2017). Seizing Control of KCC2: A New Therapeutic Target for Epilepsy. Trends Neurosci 40, 555–571. [PubMed: 28803659]

Nakano Y, Jahan I, Bonde G, Sun X, Hildebrand MS, Engelhardt JF, Smith RJ, Cornell RA, Fritzsch B, and Bánfi B (2012). A mutation in the Srrm4 gene causes alternative splicing defects and deafness in the Bronx waltzer mouse. PLoS Genet 8, e1002966. [PubMed: 23055939]

Nakano Y, Kelly MC, Rehman AU, Boger ET, Morell RJ, Kelley MW, Friedman TB, and Banfi B (2018). Defects in the alternative splicing-dependent regulation of REST cause deafness. Cell 174, 536–548.e21. [PubMed: 29961578]

Palm K, Metsis M, and Timmusk T (1999). Neuron-specific splicing of zinc finger transcription factor REST/NRSF/XBR is frequent in neuroblastomas and conserved in human, mouse and rat. Brain Res. Mol. Brain Res 72, 30–39. [PubMed: 10521596]

Patel TP, Man K, Firestein BL, and Meaney DF (2015). Automated quantification of neuronal networks and single-cell calcium dynamics using calcium imaging. J. Neurosci. Methods 243, 26–38. [PubMed: 25629800]

Phair RD, and Misteli T (2000). High mobility of proteins in the mammalian cell nucleus. Nature 404, 604–609. [PubMed: 10766243]

Popp MW, and Maquat LE (2013). Organizing principles of mammalian nonsense-mediated mRNA decay. Annu. Rev. Genet 47, 139–165. [PubMed: 24274751]

Quesnel-Vallières M, Irimia M, Cordes SP, and Blencowe BJ (2015). Essential roles for the splicing regulator nSR100/SRRM4 during nervous system development. Genes Dev 29, 746–759. [PubMed: 25838543]

Quesnel-Vallières M, Dargaei Z, Irimia M, Gonatopoulos-Pournatzis T, Ip JY, Wu M, Sterne-Weiler T, Nakagawa S, Woodin MA, Blencowe BJ, and Cordes SP (2016). Misregulation of an Activity-Dependent Splicing Network as a Common Mechanism Underlying Autism Spectrum Disorders. Mol. Cell 64, 1023–1034. [PubMed: 27984743]

Raj B, and Blencowe BJ (2015). Alternative Splicing in the Mammalian Nervous System: Recent Insights into Mechanisms and Functional Roles. Neuron 87, 14–27. [PubMed: 26139367]

Raj B, O'Hanlon D, Vessey JP, Pan Q, Ray D, Buckley NJ, Miller FD, and Blencowe BJ (2011). Cross-regulation between an alternative splicing activator and a transcription repressor controls neurogenesis. Mol. Cell 43, 843–850. [PubMed: 21884984]

Raj B, Irimia M, Braunschweig U, Sterne-Weiler T, O'Hanlon D, Lin ZY, Chen GI, Easton LE, Ule J, Gingras AC, et al. (2014). A global regulatory mechanism for activating an exon network required for neurogenesis. Mol. Cell 56, 90–103. [PubMed: 25219497]

Rivera C, Voipio J, Payne JA, Ruusuvuori E, Lahtinen H, Lamsa K, Pirvola U, Saarma M, and Kaila K (1999). The K+/Cl- co-transporter KCC2 renders GABA hyperpolarizing during neuronal maturation. Nature 397, 251–255. [PubMed: 9930699]

Author Manuscript Author Manuscript Author Manuscript Author Manuscript

Seja P, Schonewille M, Spitzmaul G, Badura A, Klein I, Rudhard Y, Wisden W, Hübner CA, De Zeeuw CI, and Jentsch TJ (2012). Raising cytosolic Cl- in cerebellar granule cells affects their excitability and vestibulo-ocular learning. EMBO J 31, 1217–1230. [PubMed: 22252133]

Shen S, Warzecha CC, Carstens RP, and Xing Y (2010). MADS+: discovery of differential splicing events from Affymetrix exon junction array data. Bioinformatics 26, 268–269. [PubMed: 19933160]

Vuong CK, Black DL, and Zheng S (2016). The neurogenetics of alternative splicing. Nat. Rev. Neurosci 17, 265–281. [PubMed: 27094079]

Westbrook TF, Hu G, Ang XL, Mulligan P, Pavlova NN, Liang A, Leng Y, Maehr R, Shi Y, Harper JW, et al. (2008). SCFbeta-TRCP controls oncogenic transformation and neural differentiation through REST degradation. Nature 452, 370–374. [PubMed: 18354483]

Wu JI, Lessard J, Olave IA, Qiu Z, Ghosh A, Graef IA, and Crabtree GR (2007). Regulation of dendritic development by neuron-specific chromatin remodeling complexes. Neuron 56, 94–108. [PubMed: 17920018]

Yang GS, Schmidt M, Yan Z, Lindbloom JD, Harding TC, Donahue BA, Engelhardt JF, Kotin R, and Davidson BL (2002). Virus-mediated transduction of murine retina with adeno-associated virus: effects of viral capsid and genome size. J. Virol 76, 7651–7660. [PubMed: 12097579]

Yeo M, Berglund K, Augustine G, and Liedtke W (2009). Novel repression of Kcc2 transcription by REST-RE-1 controls developmental switch in neuronal chloride. J. Neurosci 29, 14652–14662. [PubMed: 19923298]

Author Manuscript Author Manuscript Author Manuscript Author Manuscript

Highlights

- SRRM3 is a neuronal regulator of alternative splicing required for motor coordination
- SRRM3 and SRRM4 regulate neuronal splicing of overlapping groups of alternative exons
- SRRM3-SRRM4 activity elevates *Kcc2* expression by inactivating the gene repressor REST
- SRRM3-SRRM4 switch the GABA effect from excitatory to inhibitory by upregulating *Kcc2*

Author Manuscript Author Manuscript Author Manuscript Author Manuscript

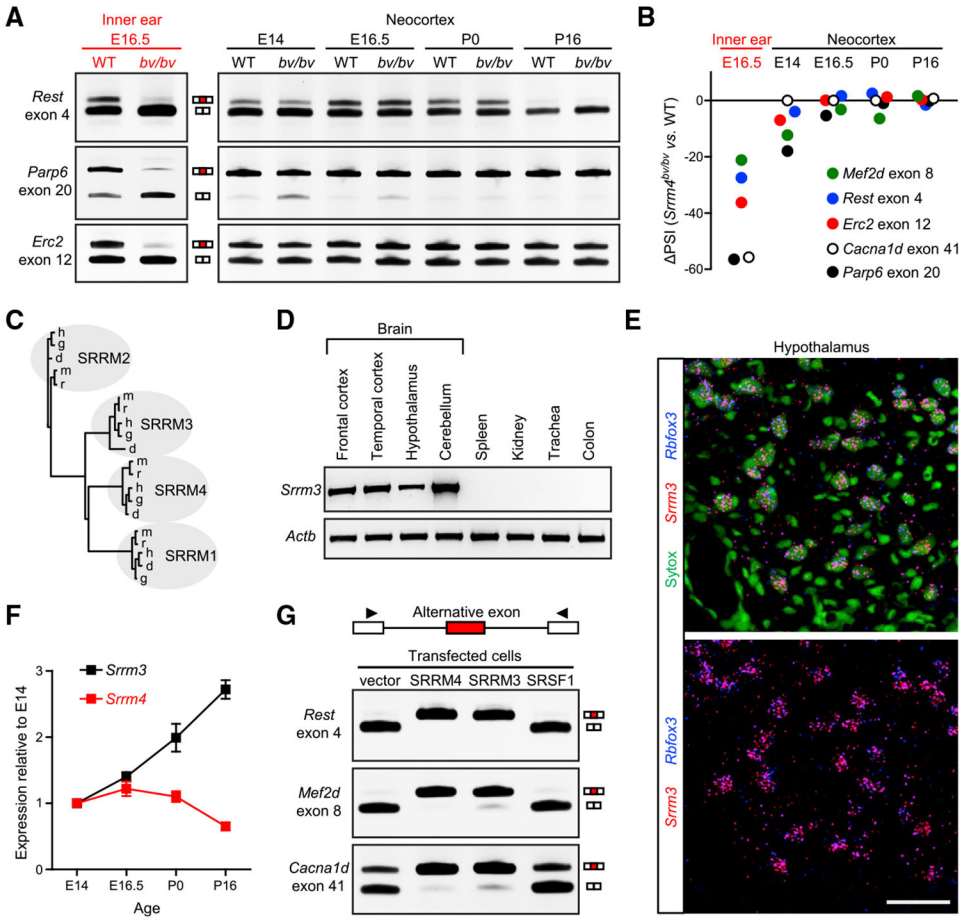

Figure 1. SRRM3 Has SRRM4-like Activity in Transfected Cells

(A) RT-PCR analysis of alternative splicing of the indicated exons in the utricular macula (inner ear) and neocortex of wild-type (WT) and *Srrm4*$^{bv/bv}$ (*bv/bv*) mice at the indicated times. Exon inclusion is depicted between gel images. RT-PCR primers were designed from constitutive exons (white boxes) flanking the tested alternative exons (red boxes).

(B) Differences in production of the long splice forms of the indicated transcripts in the inner ear and neocortex of *Srrm4*$^{bv/bv}$ versus WT mice. The long splice form of each transcript was quantified as a percentage of the total amount of that transcript (percent spliced in [PSI]). Data are based on the gel images in (A) and Figure S1A.

(C) Phylogenetic tree of SRRM proteins, constructed based on alignment of human (h), mouse (m), rat (r), dog (d), and galago (g) SRRM1–SRRM4 sequences.

(D) RT-PCR analysis of tissue distribution of *Srrm3*. Top: *Srrm3* expression. Bottom: expression of the reference gene *Actb*.

(E) Duplex *in situ* hybridization of a hypothalamic section from a WT mouse (P16) with probes complementary to *Srrm3* (red) and *Rbfox3* (blue). Cells are visualized with the nucleic acid stain Sytox (green). Scale bar, 50 μm.

(F) Changes in cortical expression of *Srrm3* and *Srrm4* from E14 to P16, as determined by qRT-PCR and shown relative to expression at E14. Values are ± SEM (n = 4 mice per time point).

Author Manuscript Author Manuscript Author Manuscript Author Manuscript

(G) RT-PCR analysis of alternative splicing in HEK293 cells co-transfected with the indicated combinations of alternative exon-encoding minigenes and splicing factors. The primers (arrowheads) were designed from constitutive exons (white boxes) flanking the alternative exons (red boxes) in the minigenes.
See also Figure S1.

Author Manuscript Author Manuscript Author Manuscript Author Manuscript

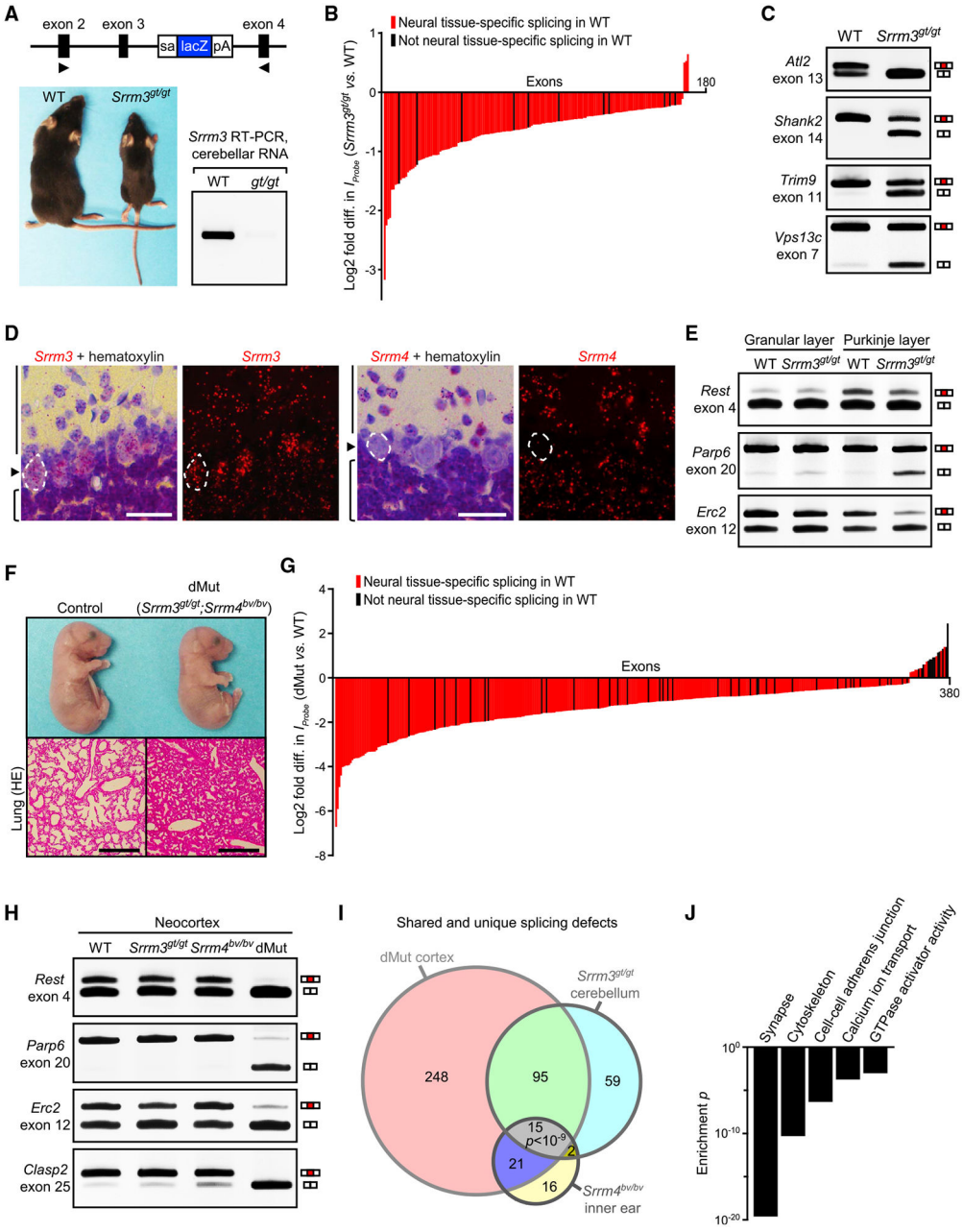

Figure 2. SRRM3 and SRRM4 Activities Overlap *In Vivo*

(A) Gene trap mutagenesis of *Srrm3*. Top: schematic of the gene trap in *Srrm3*. The splice acceptor site (sa), lacZ open reading frame, and polyadenylation site (pA) of the gene trap are indicated. Bottom left: representative image of WT and *Srrm3*$^{gt/gt}$ mice on P40. Bottom right: RT-PCR testing of *Srrm3* expression in the cerebellum of WT and *Srrm3*$^{gt/gt}$ (*gt/gt*) mice. Positions of RT-PCR primers are indicated by arrowheads at the top.

(B) Significantly different probe set signal intensities (I_{Probe}) representing 170 alternative exons in the MJAY analysis of cerebellar RNA isolated from WT and *Srrm3*$^{gt/gt}$ mice on P16. Red bars indicate alternative exons that are spliced into mature mRNA selectively in neural tissues of WT mice. Black bars indicate exons that are spliced into mature mRNA in

Author Manuscript Author Manuscript Author Manuscript Author Manuscript

both neural and non-neural tissues of WT mice. Genomic locations of the 170 exons are listed in Table S1.

(C) RT-PCR validation of 4 splicing differences in the cerebellum of WT and *Srrm3*$^{gt/gt}$ mice on P16. Additional RT-PCR validations are shown in Figure S3A.

(D) *In situ* hybridization of cerebellar sections from a WT mouse (P16) with the indicated probes. Sections were counterstained with hematoxylin. Purkinje cell somata are circled (dashed lines). The Purkinje layer (arrowheads), molecular layer (vertical lines), and granular layer (brackets) are indicated. Scale bars, 25 μm.

(E) RT-PCR testing of alternative splicing of the indicated exons in microdissected Purkinje and granular layers of the cerebellum of WT and *Srrm3*$^{gt/gt}$ mice. Additional RT-PCR tests are shown in Figure S3G.

(F) Gross morphology (top) and lung histology (H&E-stained sections, bottom) of a control (*Srrm3*$^{+/gt}$;*Srrm4*$^{bv/bv}$) and a dMut (*Srrm3*$^{gt/gt}$;*Srrm4*$^{bv/bv}$) mouse on E19. Scale bars, 200 μm.

(G) Significantly different I_{Probe} representing 379 alternative exons in the MJAY-based analysis of cortical RNA isolated from WT and dMut mice on E19. Color coding is the same as in (B). Genomic locations of the 379 exons are listed in Table S2.

(H) RT-PCR validation of 4 splicing differences in the neocortex of mice of the indicated genotypes on E19. Additional RT-PCR validations are shown in Figure S4C.

(I) Venn diagram of shared and unique splicing defects in the indicated organs of *Srrm3*$^{gt/gt}$, *Srrm4*$^{bv/bv}$, and dMut mice. The statistical significance of the 3-group overlap is shown (Monte Carlo p).

(J) Enrichment p values for representative Gene Ontology (GO) terms associated with transcripts that are differentially spliced in WT versus dMut mice.

See also Figures S2–S4, Tables S1 and S2, and Video S1.

Author Manuscript Author Manuscript Author Manuscript Author Manuscript

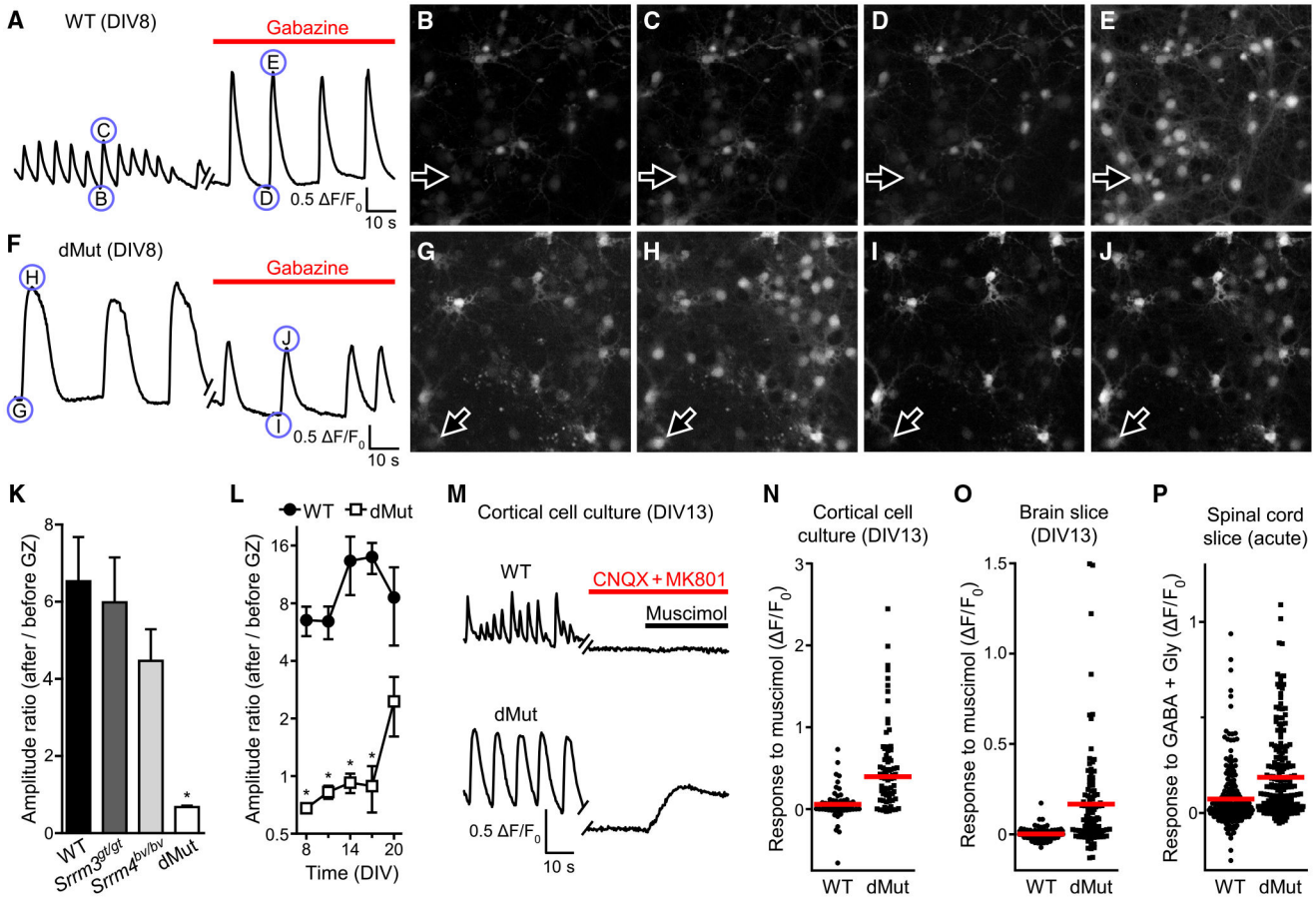

Figure 3. dMut Neurons Are Defective for the Developmental Switch in GABAergic Neurotransmission

(A–J) Gabazine (GZ)-dependent changes in Ca^{2+} oscillations in cultured cortical neurons derived from WT (A–E) and dMut (F–J) mice, as measured by Fluo-4 assay at day *in vitro* 8 (DIV8). Fluo-4 traces of individual WT (A) and dMut (F) cells are shown before and after addition of GZ (2 μM). Circled capital letters indicate points in the traces that were derived from frames shown in (B)–(E) (WT) and (G)–(J) (dMut). Arrows in (B)–(E) and (G)–(J) indicate cells whose Fluo-4 traces are shown in (A) and (F).

(K) GZ-dependent changes in the amplitudes of Ca^{2+} oscillations in cultured cortical neurons derived from mice of the indicated genotypes, as measured by Fluo-4 assay on DIV8. Values are mean ± SEM (n = 3–5 cultures isolated from 3–5 mice per genotype, one-way ANOVA p = 0.0076, Dunnett's *post hoc* test *p = 0.005, control group: WT).

(L) GZ-dependent changes in the amplitudes of Ca^{2+} oscillations in cultured cortical neurons derived from WT (closed circles) and dMut (open squares) mice, as measured by Fluo-4 assay at the indicated DIVs. Values are mean ± SEM (n = 3–9 cultures from 3–9 mice per genotype and time, unpaired Student's t test, FDR-adjusted *p < 0.05).

(M) Fluo-4 recordings of changes in Ca^{2+} concentration in a WT (top trace) and a dMut (bottom trace) cortical neuron before and after addition of CNQX and MK801 (25 μM both) and muscimol (5 μM) on DIV13.

Author Manuscript Author Manuscript Author Manuscript Author Manuscript

(N–P) Muscimol-induced (N and O) and GABA-Gly (25 μM both)-induced (P) changes in the Fluo-4 signal of CNQX-MK801-treated neurons in cortical cell cultures (N), brain slice cultures (O), and acute spinal cord slices (P) derived from WT and dMut mice on E19. The Fluo-4 recordings were made acutely (spinal cord slices) or on DIV13 (cell and slice cultures). Each symbol represents an individual cell that exhibited spontaneous Ca^{2+} oscillations before being treated with CNQX and MK801 (Mann-Whitney test $p < 0.0001$ in N, Welch's t test $p < 0.0001$ in O and P, red lines: means).
See also Figure S5.

Author Manuscript Author Manuscript Author Manuscript Author Manuscript

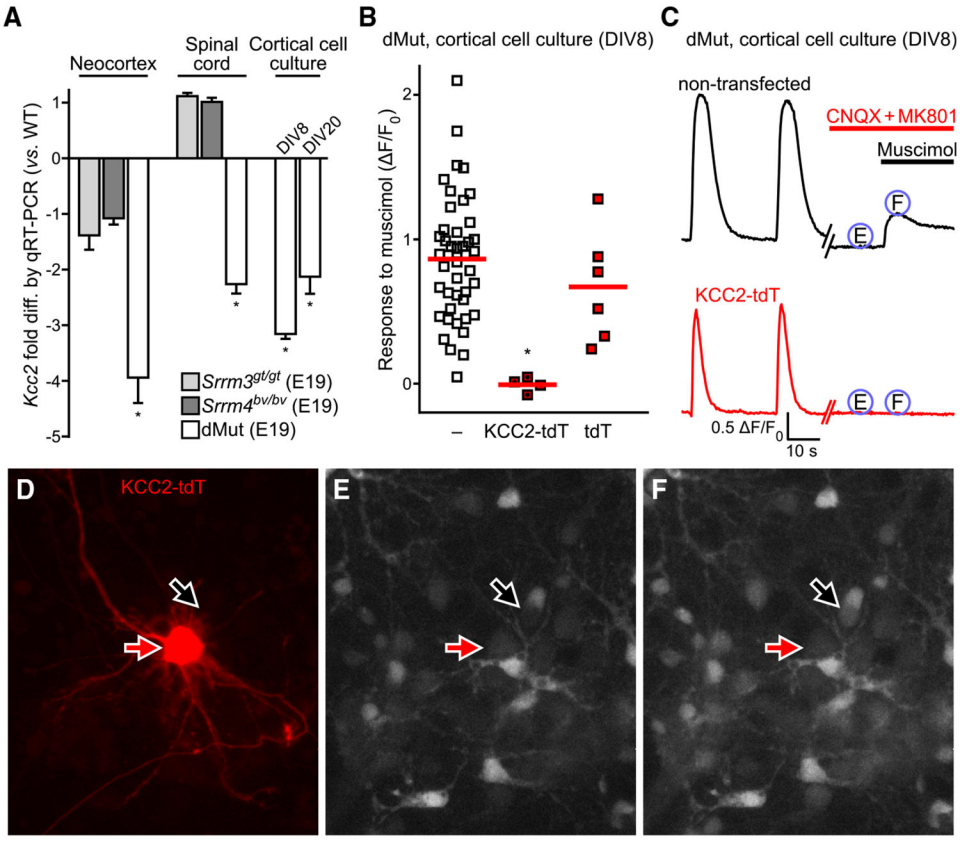

Figure 4. Transfection of dMut Neurons with *KCC2* Restores the GABAergic Switch

(A) qRT-PCR analysis of *Kcc2* expression in the neocortex, spinal cord, and cortical cell cultures from mice of the indicated genotypes. The ages of mice and cell cultures are shown. Values are mean ± SEM (n = 3–5 mice per genotype, one-sample t test, FDR-adjusted *p < 0.05, theoretical mean = |1|).

(B) Statistical analysis of muscimol-induced changes in the Fluo-4 signal of non-transfected (–), KCC2-IRES-tdTomato (KCC2-tdT)-transfected, and tdT-transfected (tdT) neurons in DIV8 cortical cell cultures derived from dMut mice. Each symbol represents an individual cell (n = 4–44 cells from 2 mice, Kruskal-Wallis test p = 0.0024, Dunn's *post hoc* test *p = 0.0014; control group: non-transfected; red lines: means).

(C–F) Muscimol-induced changes in the Fluo-4 signal of a non-transfected neuron and a KCC2-tdT-transfected neuron in a DIV8 cortical cell culture derived from a dMut mouse. Circled capital letters indicate points in the traces that were derived from the frames shown in (E) and (F). The tdT signal in the imaged field is shown in (D). Arrows in (D–F) indicate the KCC2-tdT-transfected cell (red) and the control cell (black), whose Fluo-4 traces are shown in (C).

See also Figure S6 and Table S4.

Author Manuscript Author Manuscript Author Manuscript Author Manuscript

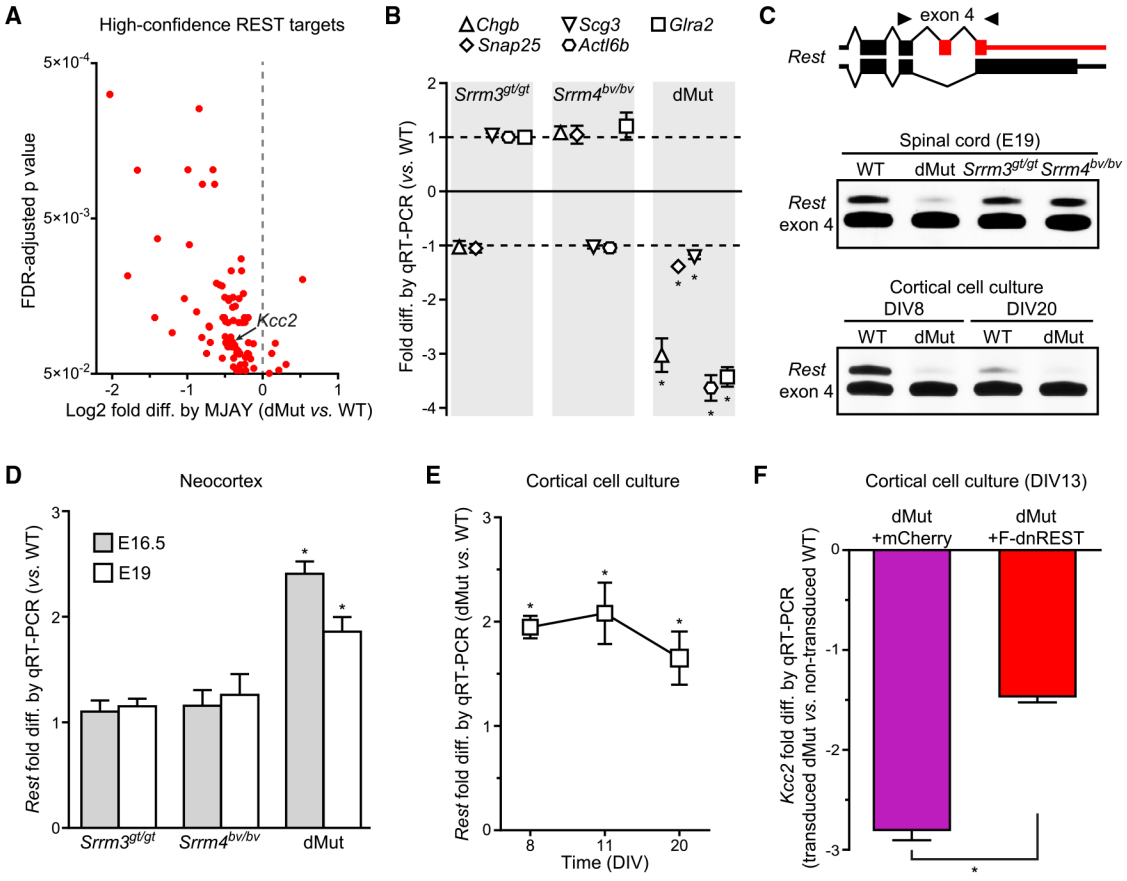

Figure 5. Defects in SRRM3-SRRM4-Dependent Regulation of REST Cause Abnormally Low Cortical Expression of *Kcc2*

(A) Volcano plot of significant differences in the cortical expression levels of high-confidence targets of REST in dMut versus WT mice on E19, as determined using MJAY. An arrow indicates the difference in *Kcc2* expression. Names of differentially expressed genes are listed in Table S3.

(B) Fold differences in the cortical expression of the indicated high-confidence target genes of REST in *Srrm3*$^{gt/gt}$, *Srrm4*$^{bv/bv}$, and dMut mice versus WT mice on E19, as determined using qRT-PCR. Values are mean ± SEM (n = 4 mice; one-sample t test, FDR-adjusted *p < 0.05; theoretical mean = |1|, indicated by dashed lines).

(C) RT-PCR analysis of the alternative splicing of exon 4 of *Rest*. Top: schematic of exon-intron structures of exon 4-containing and -omitting isoforms of *Rest*. The exon 4-dependent change in the reading frame is indicated in red. Exons (rectangles), UTRs (thin rectangles), and joining of exons in the pre-mRNA (tented lines) are shown. Arrowheads indicate positions of primers used in the RT-PCR. Center: RT-PCR analysis of the splicing of exon 4 of *Rest* in the spinal cord of mice of the indicated genotypes on E19. Bottom: RT-PCR analysis of the splicing of exon 4 of *Rest* in cortical cell cultures derived from WT and dMut mice. Cultures were analyzed on DIV8 and DIV20, as indicated.

(D) Fold difference in cortical *Rest* expression in mice of the indicated genotypes versus WT mice on E16.5 and E19, as determined using qRT-PCR. Values are mean ± SEM (n = 4 mice per genotype, one-sample t test, FDR-adjusted *p < 0.05, theoretical mean = |1|).

Author Manuscript Author Manuscript Author Manuscript Author Manuscript

(E) qRT-PCR testing of *Rest* expression in cortical cell cultures derived from WT and dMut mice and analyzed on the indicated DIVs. Values are mean ± SEM (n = 3 mice per genotype, one-sample t test, FDR-adjusted *p < 0.05, theoretical mean = 1).
(F) qRT-PCR testing of *Kcc2* expression in cortical cell cultures from dMut mice transduced with mCherry-encoding (control) or FLAG-tagged dominant-negative REST (F-dnREST)-encoding AAVs. *Kcc2* expression in non-transduced cortical cell cultures from WT mice served as a reference. Values are mean ± SEM (n = 5 mice, 2 cultures per mouse, one-sample t test, FDR-adjusted *p < 0.0002, theoretical mean = |1|.)
See also Figure S6 and Tables S3 and S4.

Author Manuscript Author Manuscript Author Manuscript Author Manuscript

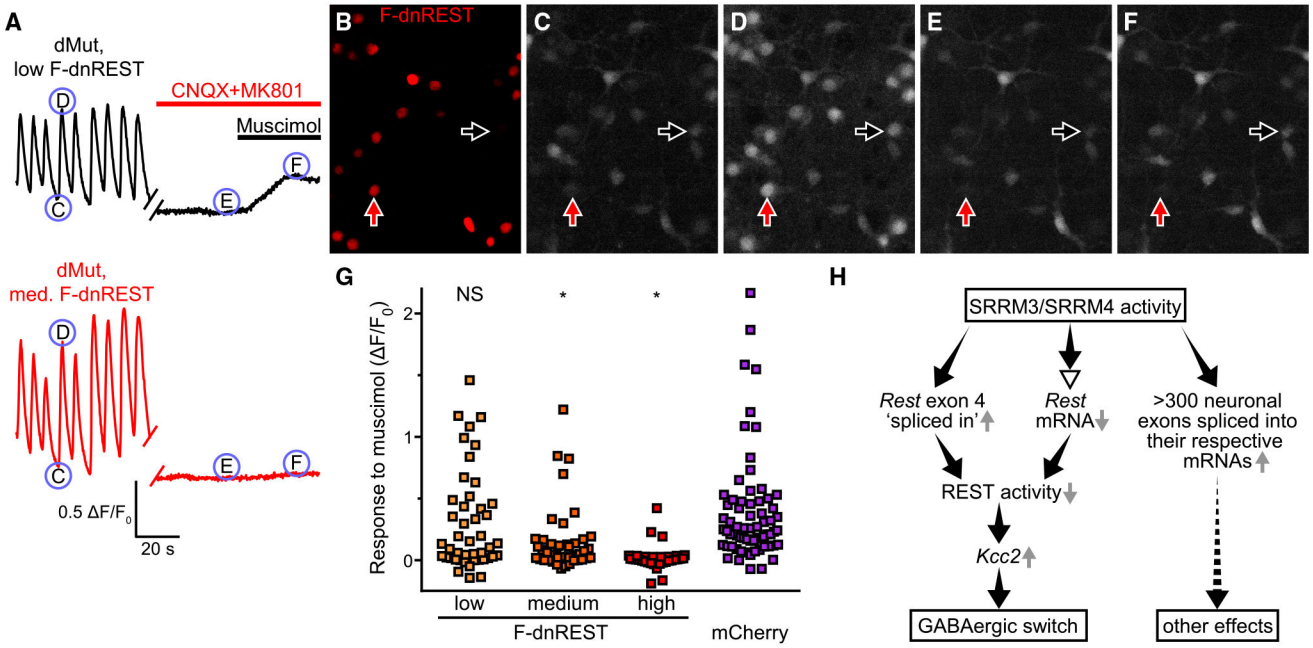

Figure 6. Forced Reduction in REST Activity Restores the GABAergic Switch in dMut Neurons

(A–F) Fluo-4 fluorescence of F-dnREST-transduced dMut cortical neurons before and during incubation with CNQX-MK801 and muscimol on DIV13. (A) shows the Fluo-4 traces of 2 representative neurons that express F-dnREST at a low level (top trace) and medium level (bottom trace). Circled capital letters indicate points in the traces that were derived from the frames shown in (C)–(F). Anti-FLAG immunofluorescence of imaged cells is shown in (B). Black arrows (low F-dnREST signal) and red arrows (medium F-dnREST signal) in (B)–(F) indicate cells whose Fluo-4 traces are shown in (A).

(G) Muscimol-induced changes in the Fluo-4 signal of F-dnREST- and mCherry-transduced dMut cortical neurons on DIV13. The muscimol-evoked Fluo-4 signals of neurons were sorted into three groups based on the intensities of anti-FLAG immunofluorescence in the same cells. Each symbol represents an individual cell (n = 32–68 cells from 2–3 mice, Kruskal-Wallis test $p < 0.0001$, Dunn's *post hoc* test *$p < 0.0001$; control group: mCherry; NS, not significant).

(H) Schematic of the SRRM3-SRRM4-dependent molecular and functional changes in cortical neurons. Black arrows indicate regulatory events tested in this study. The dashed arrow indicates non-tested regulatory connections. Gray arrows show the directions of the indicated molecular changes. The open arrowhead indicates indirect regulation.

Author Manuscript Author Manuscript Author Manuscript Author Manuscript

KEY RESOURCES TABLE

REAGENT or RESOURCE	SOURCE	IDENTIFIER
Antibodies		
Mouse anti-calbindin D-28K monoclonal antibody (clone CB-955)	Acris Antibodies	Cat# AM08219SU-N; RRID: AB_1954252
Rabbit anti-calbindin D-28K antibody	Millipore	Cat# AB1778; RRID: AB_2068336
Mouse anti-neurofilament antibody	University of Iowa Developmental Studies Hybridoma Bank	Cat# 2H3; RRID: AB_531793
Rabbit anti-Ki67 antibody (clone SP6)	Thermo Fisher Scientific	Cat# MA5–14520; RRID: AB_10979488
Mouse anti-ACTL6B antibody (clone N332B/15)	UC Davis/NIH NeuroMab Facility	Cat# 73–311; RRID: AB_2315810
Mouse anti-MAP2 antibody	Millipore	Cat# MAB364; RRID: AB_94948
Rabbit anti-LMNB1 antibody	Abcam	Cat# ab16048; RRID: AB_443298
Mouse anti-FLAG monoclonal antibody (clone M2)	Sigma	Cat# F3165; RRID: AB_259529
Alexa Fluor 488-conjugated donkey anti-mouse IgG antibody	Thermo Fisher Scientific	Cat# A-21202; RRID: AB_141607
Alexa Fluor 594-conjugated donkey anti-rabbit IgG antibody	Thermo Fisher Scientific	Cat# A-21207; RRID: AB_141637
Alexa Fluor 488-conjugated donkey anti-rabbit IgG antibody	Thermo Fisher Scientific	Cat# A-21206; RRID: AB_2535792
Alexa Fluor 568-conjugated donkey anti-mouse IgG antibody	Thermo Fisher Scientific	Cat# A10037;RRID: AB_2534013
HRP-conjugated donkey anti-rabbit IgG antibody	GE Healthcare Life Science	Cat# NA934–1ML; RRID: AB_772206
HRP-conjugated goat anti-mouse IgG antibody	Bio-Rad	Cat# 170–6516; RRID: AB_11125547
Bacterial and Virus Strains		
AAV1 with CAG-FLAG-dnREST expression cassette	Viral Vector Core Facility, University of Iowa	N/A
AAV1 with CAG-Cre-mCherry expression cassette	SignaGen Laboratories	Cat# SL101117
Chemicals, Peptides, and Recombinant Proteins		
Gabazine	Tocris Bioscience	Cat# 1262; CAS 104104-50-9
Muscimol	Sigma	Cat# M1523; CAS 2763-96-4
(+)-MK-801 hydrogen maleate	Sigma	Cat# M107; CAS 77086–22-7
CNQX disodium salt hydrate	Sigma	Cat# C239; CAS 115066-14-3
GABA	Tocris Bioscience	Cat# 0344; CAS 56-12-2
Glycine	Research Products International	Cat# G36050; CAS 56-40-6
Fluo-4, AM	Thermo Fisher Scientific	Cat# F14201; CAS 273221-67-3
HotStarTaq DNA Polymerase	QIAGEN	Cat# 203203
PerfeCTa SYBR Green FastMix	Quantabio	Cat# 95072-012
Pluronic-F127 (20% solution in DMSO)	Thermo Fisher Scientific	Cat# P3000MP
Sytox blue (5mM solution in DMSO)	Thermo Fisher Scientific	Cat# S11348
Gill's hematoxylin I	American Master Tech Scientific	Cat# HXGHE1LT
ProtectRNA RNase Inhibitor 500 × Concentrate	Sigma	Cat# R7397
Lipofectamine 3000 reagent	Thermo Fisher Scientific	Cat# L3000008
Lipofectamine LTX with PLUS reagent	Thermo Fisher Scientific	Cat# 15338100
ADVANTAGE Mounting Medium	Innovex Biosciences	Cat# NB300
Critical Commercial Assays		
SuperScript III First-Strand Synthesis System	Thermo Fisher Scientific	Cat# 18080051
Dual-Luciferase Reporter Assay System	Promega	Cat# E1910
Arcturus PicoPure Frozen RNA Isolation Kit	Thermo Fisher Scientific	Cat# KIT0204
LacZ Tissue Staining Kit	Invivogen	Cat# rep-lz-t
RNeasy Mini Kit	QIAGEN	Cat# 74104
RNeasy Micro Kit	QIAGEN	Cat# 74004
FluxOR II Green Potassium Ion Channel Assay	Thermo Fisher Scientific	Cat# F20015
View RNA ISH Tissue 2-Plex Assay kit	Thermo Fisher Scientific	Cat# QVT0012

Author Manuscript Author Manuscript Author Manuscript Author Manuscript

REAGENT or RESOURCE	SOURCE	IDENTIFIER
Nuclear Complex CoIP Kit	Active Motif	Cat# 54001
Papain dissociation system	Worthington	Cat# LK003150
NuGEN Ovation® Pico WTA System V2	NuGEN	Cat# 3302–12
FL-Ovation cDNA Biotin Module V2	NuGEN	Cat# 4200–12
WT-Ovation Exon Module	NuGEN	Cat# 2000–12
Deposited Data		
Microarray data (cerebellum, *Srrm3*$^{gt/gt}$ versus WT)	This paper	GEO: GSE71481
Microarray data (neocortex, dMut versus WT)	This paper	GEO: GSE71481
Experimental Models: Cell Lines		
HEK293 cells	ATCC	Cat# CRL-1573
N2A cells	ATCC	Cat# CCL-131
NIH3T3 cells	ATCC	Cat# CRL-1658
mIMCD-3 cells	ATCC	Cat# CRL-2123
Experimental Models: Organisms/Strains		
Mouse: B6.Cg-*Srrm3*$^{gt/gt}$	This paper	N/A
Mouse: wild-type C57BL/6J	Charles River Laboratories	Cat# 027
Mouse: *B6.Cg-Srrm4*$^{bv/bv}$	Nakano et al., 2012	N/A
Mouse: *B6.Cg-Srrm3*$^{+/gt}$;*Srrm4*$^{bv/bv}$	This paper	N/A
Oligonucleotides		
List of primers and synthetic gene fragments	Table S5	N/A
Recombinant DNA		
Exontrap Cloning Vector pET01	MoBiTec	Cat# pET01
Rest-pET	This paper	N/A
Mef2d-pET	Nakano et al., 2012	N/A
Cacna1d-pET	Nakano et al., 2012	N/A
Atl2-pET	This paper	N/A
Atl2^{M}-pET	This paper	N/A
Kif1b-pET	Nakano et al., 2012	N/A
Kif1b^{M}-pET	Nakano et al., 2012	N/A
Vsp13c-pET	Nakano et al., 2012	N/A
Vsp13c^{M1}-pET	Nakano et al., 2012	N/A
Vsp13c^{M2}-pET	Nakano et al., 2012	N/A
FLAG-mSrrm3-pcDNA3.1 +	This paper	N/A
FLAG-mSrrm4-pcDNA3.1 +	Nakano et al., 2012	N/A
FLAG-dnREST-pcDNA3.1 +	This paper	N/A
FLAG-REST 4-pLPC	Nakano et al., 2018	N/A
FLAG-REST-pLPC	Westbrook et al., 2008	Addgene 41903
SRSF1-EGFP	Phair and Misteli, 2000	Addgene 17990
CAG-KCC2-IRES-tdTomato-pCITF	Bortone and Polleux, 2009	Addgene 61404
CAG-KCC2^{Ex24-}-IRES-tdTomato-pCITF	This paper	N/A
CAG-tdTomato-pCITF	This paper	N/A
pGL4.10[luc2]	Promega	Cat# E6651
pGL4.74[hRluc/TK]	Promega	Cat# E6921
Actl6b-pGL4.10[luc2]	This paper	N/A
Actl6b^{M}-pGL4.10[luc2]	This paper	N/A
Software and Algorithms		
ImageJ2	NIH	https://imagej.net/ImageJ2; RRID: SCR_003070
Zen lite 2012	Zeiss	https://www.zeiss.com/microscopy/us/products/microscope-software/zen.html; RRID: SCR_013672

Author Manuscript

Author Manuscript

Author Manuscript

Author Manuscript

REAGENT or RESOURCE	SOURCE	IDENTIFIER
GraphPad PRISM v.7.00	GraphPad Prism	https://www.graphpad.com/scientific-software/prism/; RRID: SCR_002798
R 3.0.2	CRAN R project	https://cran.r-project.org/; RRID: SCR_001905
FluoroSNNAP software	Patel et al., 2015	https://www.seas.upenn.edu/~molneuro/software.html
UCSC Table Browser	Karolchik et al., 2004	https://genome.ucsc.edu/cgi-bin/hgTables
MATLAB	v.R2015b	https://www.mathworks.com/products/matlab.html; RRID: SCR_001622
Partek Genomics Suite	Partek, Inc	http://www.partek.com/ RRID:SCR_011860
DAVID	Huang et al., 2009	https://david.ncifcrf.gov/; RRID:SCR_001881